GLASSY MATERIALS

Structure-property relationships from universal signatures of plasticity in disordered solids

E. D. Cubuk,[1]* R. J. S. Ivancic,[2]* S. S. Schoenholz,[1,2]* D. J. Strickland,[3]* A. Basu,[2] Z. S. Davidson,[2] J. Fontaine,[4] J. L. Hor,[5] Y.-R. Huang,[5] Y. Jiang,[6] N. C. Keim,[6,7] K. D. Koshigan,[4] J. A. Lefever,[3] T. Liu,[8] X.-G. Ma,[2,9] D. J. Magagnosc,[3] E. Morrow,[10] C. P. Ortiz,[2] J. M. Rieser,[2] A. Shavit,[5] T. Still,[2] Y. Xu,[2] Y. Zhang,[8] K. N. Nordstrom,[11] P. E. Arratia,[6] R. W. Carpick,[6] D. J. Durian,[2] Z. Fakhraai,[8] D. J. Jerolmack,[12] Daeyeon Lee,[5] Ju Li,[13] R. Riggleman,[5] K. T. Turner,[6] A. G. Yodh,[2] D. S. Gianola,[14]† Andrea J. Liu[2]†

When deformed beyond their elastic limits, crystalline solids flow plastically via particle rearrangements localized around structural defects. Disordered solids also flow, but without obvious structural defects. We link structure to plasticity in disordered solids via a microscopic structural quantity, "softness," designed by machine learning to be maximally predictive of rearrangements. Experimental results and computations enabled us to measure the spatial correlations and strain response of softness, as well as two measures of plasticity: the size of rearrangements and the yield strain. All four quantities maintained remarkable commonality in their values for disordered packings of objects ranging from atoms to grains, spanning seven orders of magnitude in diameter and 13 orders of magnitude in elastic modulus. These commonalities link the spatial correlations and strain response of softness to rearrangement size and yield strain, respectively.

Disordered materials such as metallic glasses have desirable properties such as high strength and stiffness, ultrasmooth surfaces, corrosion resistance, and ultralow mechanical dissipation (*1*–*5*). Their widespread use is limited because they tend to fail in a catastrophic, brittle fashion (*6*–*9*). Brittle failure likewise hinders applications of amorphous carbon (*10*), functional nanoparticle films (*11*, *12*), and colloidal packings (*13*). These complex failure modes also limit our understanding of granular systems and symptoms of failure modes such as avalanches and earthquakes (*2*, *14*–*16*).

In many cases, the failure process starts with plastic deformation characterized by rearrangements of constituent atoms or particles. Rearrangements can occur at any strain, even when the material response appears nominally elastic, but they do not begin to play a prominent role in relaxing stress until the strain reaches the macroscopically evident yield strain. In crystalline solids, rearrangements at defects such as dislocations typically allow for plastic flow even at strains well above the yield strain, leading to a ductile response. In disordered solids, by contrast, initially localized and homogeneously distributed rearrangements often proliferate rapidly above the yield strain, coalescing to form shear bands (*6*, *17*). This process is considered the culprit behind unpredictable and often catastrophic failure.

Here, we focus on the structural underpinnings of the size of rearrangements at low strains, where rearrangements are localized and homogeneously distributed, and the magnitude of the yield strain. In crystals, most rearrangements occur at dislocations, rendering the task of linking these measures to structure relatively straightforward. For disordered solids, structural fingerprints of rearrangements are subtle. We exploit a recently introduced, machine-learned microscopic structural quantity, "softness," which has been shown to be strongly predictive of rearrangements in disordered solids (*18*) and has expanded our conceptual understanding of glassy liquids (*19*, *20*) and aging glasses (*21*). We link the spatial correlations of softness to the size of rearrangements, and we link the strain response of softness to the yield strain.

We conducted experiments and simulations on a range of materials including amorphous carbon, silica, metallic glasses, small-molecule and oligomeric glasses, nanoparticle packings, colloidal systems, aqueous foams, and granular packings (*22*) (see figs. S2 to S4, S6, S7, and S10 to S12). In many of these systems, the interparticle interactions are purely repulsive, whereas in others there is metallic, covalent, or van der Waals bonding. Some of the systems are two-dimensional (2D), but most are 3D. Moreover, the rearrangements have differing origins. In packings of atoms, molecules, and smaller colloids, thermal fluctuations can induce rearrangements even in the absence of any mechanical load. Under applied load, both the incurred stress and the temperature can contribute to rearrangements. In aqueous foams, which are disordered packings of air bubbles, some of the rearrangements are induced by load while others are caused by the coarsening process, in which large bubbles grow at the expense of smaller ones. In larger colloids and granular packings, all of the rearrangements are induced by the applied load. We consider a variety of loading geometries including indentation, uniaxial loading of pillars under extension or tension, and simple shear.

Common rearrangement size in disordered solids

We begin by characterizing the size of rearrangements, which are the precursors to global plasticity. Rearrangements (or the initial rearrangements in an avalanche) have been recognized as being localized in systems such as Lennard-Jones glasses (*23*), bubble rafts (*24*), foams (*25*), and colloidal glasses (*26*). Frameworks such as shear transformation zone theory start with the assumption that rearrangements are localized (*23*, *27*). Nonetheless, a consistent quantitative measure of their size has been lacking. For systems in which we can obtain the particle positions in real space as a function of time, namely colloidal and granular packings or computational models, it is essential to distinguish rearrangements from other types of displacements without specifying the nature of the rearrangement. To do so, we follow the literature and evaluate the quantity D^2_{min} between times t and $t + \Delta t$ (*23*). This quantity captures the mean square deviation of a particle's position from the best-fit affine deformation of its neighborhood,

$$D^2_{\mathrm{min}} = \frac{1}{M_k}\sum_{i}^{M_k}[\mathbf{r}_{ik}(t+\Delta t) - \mathbf{J}_k(t)\mathbf{r}_{ik}(t)]^2 \quad (1)$$

[1]Google Brain, Mountain View, CA 94043, USA. [2]Department of Physics and Astronomy, University of Pennsylvania, Philadelphia, PA 19104, USA. [3]Department of Materials Science and Engineering, University of Pennsylvania, Philadelphia, PA 19104, USA. [4]Laboratoire de Tribologie et Dynamique des Systémes, École Centrale de Lyon, CNRS UMR 5513, Université de Lyon, 69134 Ecully Cedex, France. [5]Department of Chemical and Biomolecular Engineering, University of Pennsylvania, Philadelphia, PA 19104, USA. [6]Department of Mechanical Engineering and Applied Mechanics, University of Pennsylvania, Philadelphia, PA 19104, USA. [7]Physics Department, California Polytechnic State University, San Luis Obispo, CA 93407, USA. [8]Department of Chemistry, University of Pennsylvania, Philadelphia, PA 19104, USA. [9]Complex Assemblies of Soft Matter, CNRS-Solvay-UPenn UMI 3254, Bristol, PA 19007, USA. [10]Department of Physics, Houghton College, Houghton, NY 14744, USA. [11]Department of Physics, Mount Holyoke College, South Hadley, MA 01075, USA. [12]Department of Earth and Environmental Sciences, University of Pennsylvania, Philadelphia, PA 19104, USA. [13]Department of Nuclear Science and Engineering and Department of Materials Science and Engineering, Massachusetts Institute of Technology, Cambridge, MA 02139, USA. [14]Materials Department, University of California, Santa Barbara, CA 93106, USA.
*These authors contributed equally to this work.
†Corresponding author. Email: ajliu@physics.upenn.edu (A.J.L.); gianola@engr.ucsb.edu (D.S.G.)

and therefore measures the nonaffine motion of particle k at time t (*23*). Here, $\mathbf{r}_{ik}(t)$ is the displacement vector between particles i and k at time t, $\mathbf{J}_k(t)$ is the "best-fit" local deformation gradient tensor about particle k that minimizes $D^2_{\mathrm{min}}(k;t)$, and the summation runs over the M_k particles within a radius R_c^D of particle k.

To measure the spatial extent of rearrangements, we consider the normalized correlation function

$$\langle \delta D^2_{\mathrm{min}}(0)\delta D^2_{\mathrm{min}}(r)\rangle \equiv \frac{\langle D^2_{\mathrm{min}}(0)D^2_{\mathrm{min}}(r)\rangle - \langle D^2_{\mathrm{min}}\rangle^2}{\langle [D^2_{\mathrm{min}}]^2\rangle - \langle D^2_{\mathrm{min}}\rangle^2} \quad (2)$$

Note that the result depends on the time interval Δt used to define D^2_{min}. Many of the systems we study exhibit avalanches near yielding, where an initial localized rearrangement can trigger others, leading to a cascade. To focus on the initial rearrangement, we calculate D^2_{min} at the value of Δt corresponding to the minimum of the correlation length ξ_r (*22*) (see fig. S1). It also depends on the size of the neighborhood R_c^D; we find that ξ_r is insensitive to R_c^D as long as it lies somewhere between the first and second peaks of the pair correlation function, $g(r)$ (*22*) (see fig. S1). Figure 1A demonstrates the exponential decay of $\langle \delta D^2_{\mathrm{min}}(0)\delta D^2_{\mathrm{min}}(r)\rangle$ with r in units of the particle diameter d for two different systems selected from our broader study: a 3D melt of short polymer chains, in which the diameter d corresponds to the size of a monomer, and a 2D bidisperse granular pillar, where d represents the diameter of the larger particles. Indeed, for all of the experimental and computational systems studied, we find that the correlations are reasonably well described by an exponential decay with a correlation length ξ_r (see figs. S2B, S3B, S5B, S8B, and S9B). We therefore characterize the size of rearrangements by ξ_r. Note that this length scale is distinct from that associated with dynamical heterogeneities near the glass transition (*28*). The first quantity is obtained from D^2_{min} calculated over a microscopic time scale; the second quantity is measured over a longer time period and is considerably larger because an initial rearrangement of size ξ_r can spread in avalanche fashion (*29*).

In crystalline systems, rearrangements are concentrated at crystalline defects and therefore reflect spatial correlations associated with the dimensionality and spatial extent of the specific defects. Planar defects such as grain boundaries delineate crystal-crystal interfaces, whereas linear defects such as dislocations can take on complex and spatially extended configurations with a multitude of characters (edge, screw, or mixed). These details can vary enormously from one crystalline system to another and will inevitably affect ξ_r. Furthermore, not all crystalline defects can produce plastic strain (e.g., immobile grain boundaries). We therefore do not expect any commonality in the value of ξ_r for crystalline systems.

Our analysis of disordered solids draws a striking contrast. Overall we have studied 12 different systems. For six of these systems, which span almost the entire range covered by the 12 systems in terms of Young's modulus, particle size, and particle interactions, we have obtained the particle position versus time data needed for the analysis of rearrangement size. Specifically, three of these systems are computational disordered solids, all in 3D [the van Beest, Kramer, and van Santen (BKS) silica model (*30*), the Kob-Andersen model of a Lennard-Jones glass (*31*), and oligomer glass pillars (*32*)] and three are experimental disordered solids [3D colloidal pillars, 2D granular pillars, and 2D poly(*N*-isopropyl acrylamide) (PNIPAM) colloid glasses]. Figure 2A compiles our results for ξ_r versus particle diameter. The results fall very close to the line of best fit, ξ_r/d = 1.1 ± 0.2, where d is the effective particle diameter (*22*). In the inset of Fig. 2A, we show the ratio ξ_r/d for the same systems on a log-linear scale; this more unforgiving way of plotting our results shows the adherence to a common value of ξ_r/d.

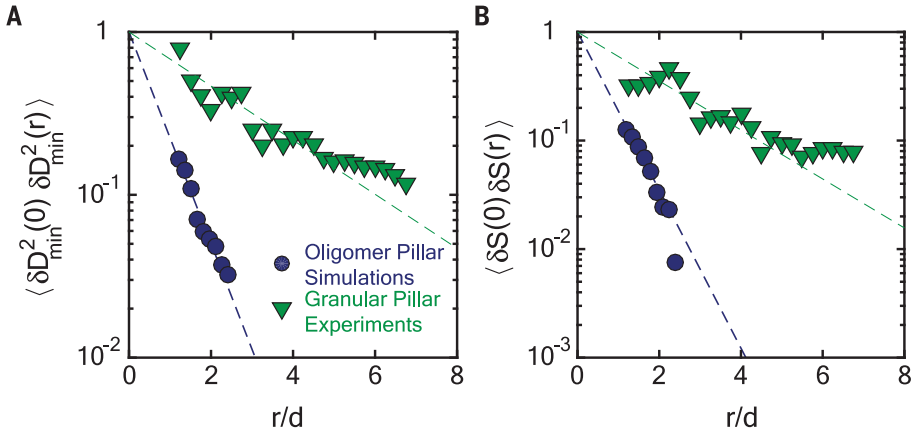

Fig. 1. Spatial correlations in D^2_{min} and softness fields. (**A** and **B**) Spatial correlations in the D^2_{min} field (A) and softness field (B) for two very different systems: a 3D short-chained polymer pillar studied by molecular dynamics simulation (circles) and a 2D bi-dispersed granular pillar studied experimentally (triangles). Here, d is the diameter of a single monomer for the polymer pillar and of a large particle for the granular pillar, and r is the radial distance. The dashed lines are fits to $\exp(-r/\xi_r)$ in (A) and to $\exp(-r/\xi_s)$ in (B), defining the size of rearrangements, ξ_r, and of soft regions, ξ_s. Similar exponential decays hold for all other systems studied (*22*).

Linking softness to rearrangements

Mounting evidence has shown that rearrangements across a wide array of disordered materials depend on local structure and energetics (*33*–*37*). It has been shown that local yield stress is an excellent predictor of rearrangements in athermal glasses (*37*). However, calculation of local yield stress requires knowledge of interparticle interactions; this is often difficult to obtain in experimental systems such as colloidal and granular packings, which are naturally polydisperse. Several of us (*19*, *21*) have shown that local structure alone can be used to develop a predictive description of dynamics in glassy liquids (*19*) and aging glasses (*21*). Central to the approach is the introduction of "softness," a particle-based quantity that depends only on the local structural environment of the particle. Thus, softness can be determined from any static picture (or snapshot) of the structure along deformation, time, or temperature trajectories. Softness is essentially a weighted integral over the local pair correlation function $g_i(r)$ (*20*). Using a machine-learning approach akin to linear regression (*22*), the weighting function is designed to optimize the prediction accuracy for rearrangements (*19*). In Lennard-Jones glasses (*19*) and oligomer glasses (*38*), it has been shown that the energy barrier that must be surmounted for the particle to rearrange decreases linearly with increasing softness. Thus, rearrangements are exponentially more likely to involve particles with high softness. Note that just as not all dislocations contribute to plasticity in crystals, not all high-softness particles participate in rearrangements; like particles surrounding dislocations, soft particles are simply more likely to rearrange than others.

Because high-softness particles are much more likely to rearrange, one would expect the size of a rearrangement to be limited by the spatial extent of high-softness regions. In analogy to the previous discussion of D^2_{min}, we quantify the size of structural heterogeneities by considering the normalized spatial correlation function,

$$\langle \delta S(0)\delta S(r)\rangle \equiv \frac{\langle S(0)S(r)\rangle - \langle S\rangle^2}{\langle S^2\rangle - \langle S\rangle^2} \quad (3)$$

As with D^2_{min}, we find that $\langle \delta S(0) \delta S(r) \rangle$ decays approximately exponentially with the correlation length ξ_s, as shown in Fig. 1B for the short-chain polymer glass and granular pillar. Similar plots for the other four systems studied are shown in figs. S2B, S3B, S5A, S8A, and S9A. Thus, ξ_s is a good measure of the size of high-softness regions that are more likely to rearrange. We find that the emergent correlations of S are nearly universal: Fig. 2B shows that like the rearrangement size ξ_r, the spatial correlation length for softness (the size of soft regions), ξ_s, falls on a common line $\xi_s/d = 1.1 \pm 0.2$ for all systems studied. Thus, ξ_r and ξ_s are strongly correlated. We now ask whether ξ_s is comparable to the size of rearrangements, ξ_r. In Fig. 2C we show the ratio of the size of rearrangements to the size of soft regions, ξ_r/ξ_s. Indeed, we find $\xi_r/\xi_s = 0.97 \pm 0.07$, with a scatter in ξ_r/ξ_s that is significantly smaller than for ξ_r/d or ξ_s/d, even while ξ_r and ξ_s individually vary by more than seven orders of magnitude. Our multiscale analysis provides compelling evidence that the size of rearrangements, ξ_r, is encoded in the size of correlated soft regions in the system, ξ_s, independent of the nature and even the sign of interactions, the dimensionality of the system, and how the rearrangements were induced.

Common yield strain in disordered solids

We next asked whether commonality of plasticity is observed only in microscopic measures (i.e., rearrangement size and softness correlation length) or whether it is also present in macroscopic measures, such as the strain at the onset of yielding. In crystalline systems, the yield strain is strongly dependent on microstructural details. Only in the limit of ideal strength (the theoretical upper limit) is a constant yield strain expected, as a result of the cooperative crystal shearing mechanism needed in this extreme. In crystalline engineering materials, preexisting defects are plentiful and thus the yield strain depends strongly on processing. A common practice in selection of materials for engineering design is to populate a plot of yield strength versus Young's modulus E. Slopes drawn on such an "Ashby chart" give one measure of the yield strain. As a basis for comparison, we examined values for crystalline systems categorized by material class, represented in Fig. 3 as clouds. The yield strength of crystalline metals varies by nearly four orders of magnitude despite a relatively small variation in E. Semicrystalline polymers, on the other hand, show a relatively small variation in yield strength yet can exhibit large differences in E. Clearly, there is no universality in the onset of yielding in crystalline systems, either within a particular material class or overall.

In contrast, it is known that certain classes of disordered materials share a common value of the yield strain (*39*–*41*) despite the heterogeneity of atomic or particle positions within the material. A constant value of the yield strain in shear of 2.7% was empirically shown for a set of metallic glasses on the basis of mechanical tests (*39*) and was further corroborated by atomistic simulations (*40*). Experiments on uniaxially loaded colloidal pillars showed a similar yield strain even though the elastic moduli were smaller by as much as five orders of magnitude (*41*).

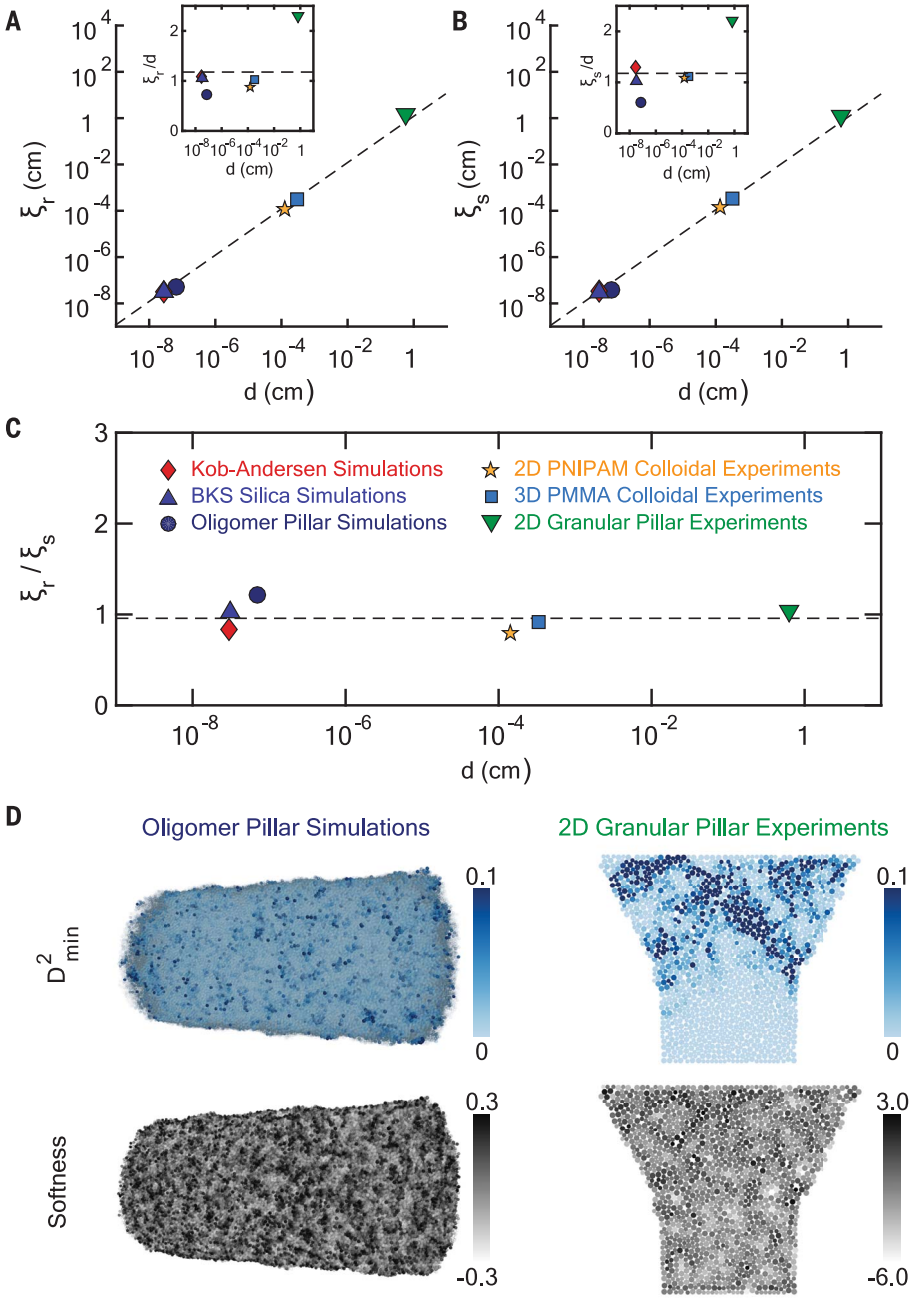

Fig. 2. Microscopic analysis of dynamics and structure. Emergent properties of the D^2_{min} and softness fields for six different materials are shown, as indicated within (C). (**A** and **B**) The correlation lengths of D^2_{min} (A) and softness (B), ξ_r and ξ_s respectively, are plotted against particle diameter d for each material on a log-log scale. The dashed lines in (A) and (B) represent the proportionality relations $\xi_r/d = 1.1 \pm 0.2$ and $\xi_s/d = 1.1 \pm 0.2$, respectively. The insets show ξ_r/d and ξ_s/d, respectively, versus d on a log-linear scale. (**C**) The ratio ξ_r/ξ_s is plotted against d for each material on a log-linear scale. The average of this ratio is $\xi_r/\xi_s = 0.97 \pm 0.07$ (dashed line). (**D**) Snapshots of the D^2_{min} and softness fields for the oligomer pillar simulation and the granular pillar experiment.

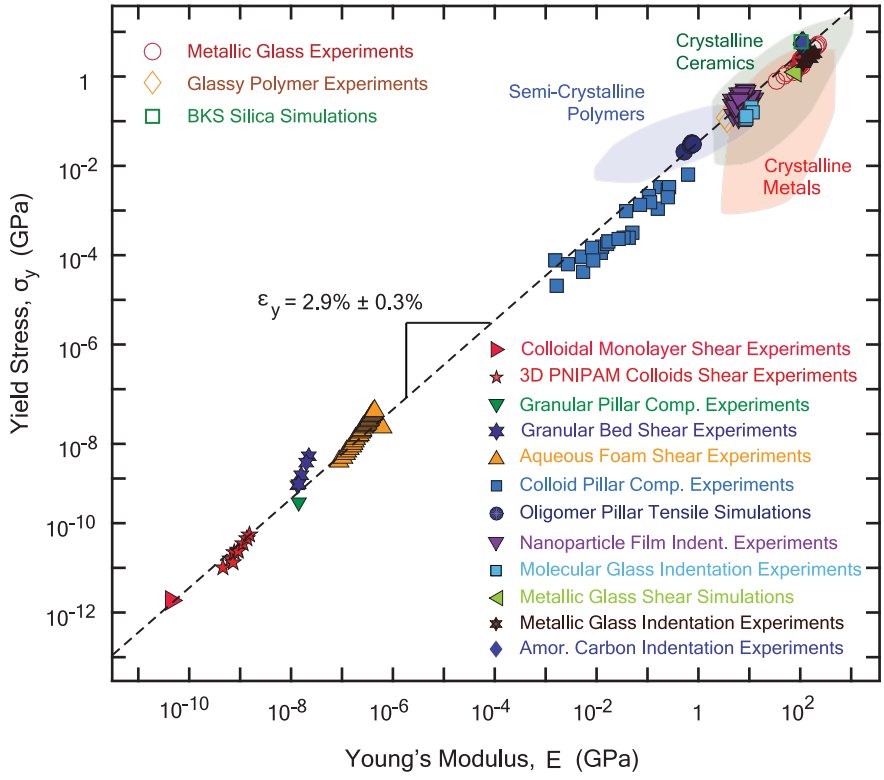

Fig. 3. Macroscopic mechanical response. An Ashby chart shows yield stress σ_y versus Young's modulus E for a variety of experimental and simulated disordered systems. We also include literature values for metallic glass experiments (*39*), glassy polymer experiments (*42*), and BKS silica simulations (*43*). The data collapse onto a single curve, implying a universal yield strain of ε_y = 2.9 ± 0.3% (dashed line). In contrast, crystalline metals (red cloud) show a large variation in strength with little change in E, and semicrystalline polymers (blue cloud) show a wide variation in E with little change in strength. Previously reported crystalline material clouds were generated using Materials Property CES Selector software by Granta Design.

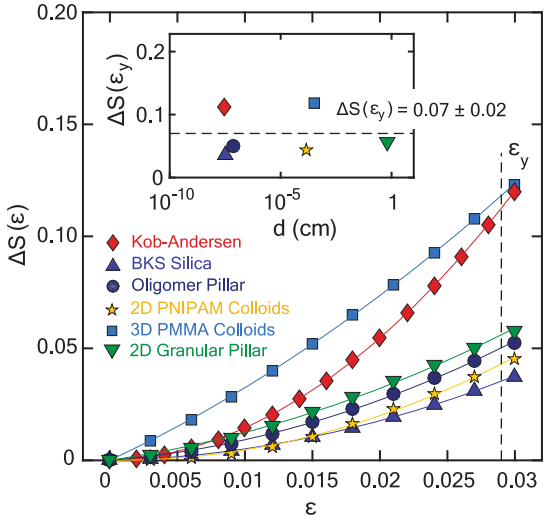

Fig. 4. Response of softness to affine strain. The response of the mean softness to an affine uniaxial extension, ε, for six different materials is quantified using $\Delta S(\varepsilon) = [\langle S(\varepsilon)\rangle - \langle S(0)\rangle]/\sigma_S$, where $\langle S(\varepsilon)\rangle$ is the mean softness at a strain of ε and σ_S is the standard deviation of softness at a strain of ε = 0. These data were obtained by applying a uniaxial extension of magnitude ε to the neighborhood about each particle larger than the one used to calculate softness in each material. The softness field for the strained material was calculated using the original hyperplane and then averaged. The dashed line denotes the universal value of yield strain for disordered materials, ε_y. The inset shows values of $\Delta S(\varepsilon_y)$ versus particle diameter d for all six systems. These values are all similar, suggesting that the universality of the yield strain of disordered materials reflects a common response of softness to strain.

Here, we extend the Ashby chart for disordered solids from five orders of magnitude (*41*) to more than 13 orders of magnitude in elastic modulus. To do this, we have expanded the class of disordered systems to include covalently bonded amorphous solids (amorphous carbon) and several different metallic glasses (see table S1) as well as extremely weakly attracting or purely repulsive systems (colloids, aqueous foams, and granular materials; see tables S2 and S3). We include experimental and computational results for systems subjected to various loading conditions (uniaxial compression/tension, indentation, and shear). Figure 3 shows our collated results for yield strength versus E. Strikingly, the data collapse onto a single line on this log-log plot with a linear relationship, corresponding to a universal yield strain of ε_y = 2.9 ± 0.3%. Note that the data collapse is insensitive to the specific definition of the yield strain, as detailed for each system (*22*). We also include literature values for metallic glasses (*39*), glassy polymers (*42*), and simulations of silica (*43*), which also collapse on the universal curve. We note that although microscopic information is not available in all systems shown in Fig. 3, four of the systems spanning nearly the full range of E values appear in both Figs. 2 and 3. The implication of this result is that the macroscopic shape change (kinematics) needed for the onset of yield is essentially universal in disordered materials, irrespective of the nature of the interparticle or atomic interactions.

Linking softness to yield strain

To draw a link between the yield strain and microscopic structure as quantified by softness, we draw insight from results for glass-forming liquids by noting an analogy between the yield strain ε_y and the glass transition temperature T_g. They respectively mark the strain and temperature at which rearrangements relax the system on the time scale of measurement. In thermal glassy liquids, the average softness $\langle S\rangle$ is controlled by temperature T; the higher T, the higher $\langle S\rangle$ (*19*). Moreover, it has been shown that there is a relation between relaxation time and $\langle S\rangle$; the higher $\langle S\rangle$, the shorter the relaxation time (*21*). The shift in $\langle S\rangle$ with T thus provides a structural measure that tells us about the sensitivity of the relaxation time to temperature.

We suggest that the sensitivity of $\langle S\rangle$ to strain ε provides a way of understanding the common value of the yield strain across systems. We consider a neighborhood around particle k that is larger than the neighborhood required to calculate softness, and apply an affine uniaxial extension at fixed volume (pure shear) of magnitude ε to the neighborhood. We then recalculate softness for particle k. The result averaged over all particles is $\langle S(\varepsilon)\rangle$; we also calculate the standard deviation of the softness distribution in the absence of strain, $\sigma_S = \sqrt{\langle S^2\rangle - \langle S\rangle^2}$. The quantity $\Delta S(\varepsilon) \equiv [\langle S(\varepsilon)\rangle - \langle S(0)\rangle]/\sigma_S$ measures the

change of softness due to applied strain in units of the standard deviation of the softness distribution.

Figure 4 shows that $\Delta S(\varepsilon)$ increases with strain ε, indicating an increased likelihood of rearrangements with strain, as expected. A value of $\Delta S(\varepsilon) = 1$ would correspond to a shift of the average softness equal to the standard deviation of the softness distribution. Note that the shift in average softness is an order of magnitude smaller than the standard deviation for all systems over the range of strains studied. The response of softness to strain is characterized by a smooth function that is quite similar quantitatively for all six systems up to (and even beyond) the onset of macroscopic yielding. The inset of Fig. 4 shows the value of $\Delta S(\varepsilon)$ at the common value of the yield strain ε_y as determined from Fig. 3, demonstrating commonality across length scales. This quantitative similarity of the response of softness to strain for all systems studied provides strong evidence that commonality of yield strain has an underlying structural origin.

Discussion

Figures 2, 3, and 4 provide evidence of universality of spatial correlations in the microscopic dynamics and structure connected to plasticity, as well as universality in the onset of macroscopic yielding and in the response of microscopic structure to strain in disordered solids. These quantitative commonalities transcend the details of constituent size and interactions.

The observed universality lends quantitative credence to the use of model disordered solids as analogs of atomic glasses—for instance, in sheared bubble rafts (*24*) and colloidal solids (*26*). Commonalities in the statistics of slip intermittency just above yield among various disordered solids (*44*, *45*) suggest additional universality near yield. One corollary of commonality of yield strain is that one cannot easily increase the strain at the onset of yielding of a disordered solid. A more promising route to increasing the toughness of disordered solids may be to manipulate the evolution of rearrangements above the yield strain, thereby increasing the window of plastic flow between the yield strain and failure. The success of the softness framework in explaining two properties of plasticity near yield suggests that it may also provide a fruitful approach for studying shear band formation in systems beyond yield.

The universal behaviors that we observe are all the more striking because there is no sign of universality in the microscopic packing structure itself. For each system, the definition of softness is different. Universality only becomes apparent once the softness of the constituent particles is considered, where we see emergent commonality in the properties of softness.

In crystals, on the other hand, there is universality in the microscopic structure, in the sense that there is a universal definition of a dislocation independent of constituent size, interactions, or crystal structure. However, the spatial correlations of dislocations vary enormously from one crystalline system to another—a direct consequence of the extended nature of these linear defects. As a result, the emergent properties of crystalline defects are not universal. There is no commonality in the spatial correlations of dislocations, so we expect no commonality in the spatial size of rearrangement events. Likewise, there is no commonality in the yield strain among material classes (Fig. 3). Indeed, most efforts in the modeling of crystal plasticity focus on incorporating specific features of the material under study (e.g., dislocation density and character of dislocations) and the prevailing notion is that no unifying theory is tractable.

The essential differences between plasticity in crystals and plasticity in disordered materials can be summarized as follows. In crystals, there is universality in the definition of the microscopic structural features correlated with rearrangements, but in disordered solids there is not. On the other hand, in disordered solids there is emergent universality in the properties of those features, but in crystals there is not. The origin of this universality is not yet understood. Our results, however, point to the possibility of a unifying framework and a vast simplification of our understanding of plasticity in disordered solids, which paradoxically may not be possible for crystals.

REFERENCES AND NOTES

1. M. M. Trexler, N. N. Thadhani, *Prog. Mater. Sci.* **55**, 759–839 (2010).
2. H. M. Jaeger, S. R. Nagel, R. P. Behringer, *Rev. Mod. Phys.* **68**, 1259–1273 (1996).
3. N. P. Bansal, R. H. Doremus, *Handbook of Glass Properties* (Academic Press, 1986).
4. K. E. Parmenter, F. Milstein, *J. Non-Cryst. Solids* **223**, 179–189 (1998).
5. L. E. Nielson, R. F. Landel, *Mechanical Properties of Polymers and Composites*, vol. 2 (Marcel Dekker, 1981).
6. C. A. Schuh, T. C. Hufnagel, U. Ramamurty, *Acta Mater.* **55**, 4067–4109 (2007).
7. M. Chen, *Annu. Rev. Mater. Res.* **38**, 445–469 (2008).
8. F. Barthelat, R. Rabiei, *J. Mech. Phys. Solids* **59**, 829–840 (2011).
9. R. O. Ritchie, *Nat. Mater.* **10**, 817–822 (2011).
10. J. Robertson, *Mater. Sci. Eng. Rep.* **37**, 129–281 (2002).
11. J. Herrmann *et al.*, *Appl. Phys. Lett.* **91**, 183105 (2007).
12. L. Zhang *et al.*, *ACS Nano* **7**, 8043–8050 (2013).
13. P. C. Hiemenz, *Principles of Colloid and Surface Chemistry* (Marcel Dekker, ed. 2, 1986).
14. R. M. Nedderman, *Statics and Kinematics of Granular Materials* (Cambridge Univ. Press, 1992).
15. D. Gidaspow, *Multiphase Flow and Fluidization: Continuum and Kinetic Theory Descriptions* (Academic Press, 1994).
16. H. J. Herrmann, J. P. Hovi, S. Luding, *Physics of Dry Granular Media* (Kluwer Academic, 1998).
17. A. Greer, Y. Cheng, E. Ma, *Mater. Sci. Eng. Rep.* **74**, 71–132 (2013).
18. E. D. Cubuk *et al.*, *Phys. Rev. Lett.* **114**, 108001 (2015).
19. S. S. Schoenholz, E. D. Cubuk, D. M. Sussman, E. Kaxiras, A. J. Liu, *Nat. Phys.* **12**, 469–471 (2016).
20. E. D. Cubuk, S. S. Schoenholz, E. Kaxiras, A. J. Liu, *J. Phys. Chem. B* **120**, 6139–6146 (2016).
21. S. S. Schoenholz, E. D. Cubuk, E. Kaxiras, A. J. Liu, *Proc. Natl. Acad. Sci. U.S.A.* **114**, 263–267 (2017).
22. See supplementary materials.
23. M. L. Falk, J. S. Langer, *Phys. Rev. E* **57**, 7192–7205 (1998).
24. A. Argon, H. Kuo, *Mater. Sci. Eng.* **39**, 101–109 (1979).
25. D. J. Durian, D. A. Weitz, D. J. Pine, *Science* **252**, 686–688 (1991).
26. P. Schall, D. A. Weitz, F. Spaepen, *Science* **318**, 1895–1899 (2007).
27. M. L. Falk, J. S. Langer, *Annu. Rev. Condens. Matter Phys.* **2**, 353–373 (2011).
28. L. Berthier, G. Biroli, J.-P. Bouchaud, L. Cipelletti, W. van Saarloos, *Dynamical Heterogeneities in Glasses, Colloids, and Granular Media* (Oxford Univ. Press, 2011).
29. R. Candelier *et al.*, *Phys. Rev. Lett.* **105**, 135702 (2010).
30. B. W. H. van Beest, G. J. Kramer, R. A. van Santen, *Phys. Rev. Lett.* **64**, 1955–1958 (1990).
31. W. Kob, H. C. Andersen, *Phys. Rev. Lett.* **73**, 1376–1379 (1994).
32. A. Shavit, R. A. Riggleman, *Phys. Chem. Chem. Phys.* **16**, 10301–10309 (2014).
33. C. Brito, M. Wyart, *J. Stat. Mech.* **2007**, L08003 (2007).
34. D. J. Ashton, J. P. Garrahan, *Eur. Phys. J. E* **30**, 303–307 (2009).
35. J. Rottler, S. S. Schoenholz, A. J. Liu, *Phys. Rev. E* **89**, 042304 (2014).
36. S. S. Schoenholz, A. J. Liu, R. Riggleman, J. Rottler, *Phys. Rev. X* **4**, 031014 (2014).
37. S. Patinet, D. Vandembroucq, M. L. Falk, *Phys. Rev. Lett.* **117**, 045501 (2016).
38. D. M. Sussman, S. S. Schoenholz, E. D. Cubuk, A. J. Liu, *Proc. Natl. Acad. Sci. U.S.A.* **114**, 10601–10605 (2017).
39. W. L. Johnson, K. Samwer, *Phys. Rev. Lett.* **95**, 195501 (2005).
40. Y. Q. Cheng, A. J. Cao, H. W. Sheng, E. Ma, *Acta Mater.* **56**, 5263–5275 (2008).
41. D. J. Strickland, Y.-R. Huang, D. Lee, D. S. Gianola, *Proc. Natl. Acad. Sci. U.S.A.* **111**, 18167–18172 (2014).
42. V. V. Kozey, S. Kumar, *J. Mater. Res.* **9**, 2717–2726 (1994).
43. C. Tang, L. P. Da'vila, *J. Appl. Phys.* **118**, 094302 (2015).
44. J. T. Uhl *et al.*, *Sci. Rep.* **5**, 16493 (2015).
45. D. V. Denisov, K. A. Lörincz, J. T. Uhl, K. A. Dahmen, P. Schall, *Nat. Commun.* **7**, 10641 (2016).

ACKNOWLEDGMENTS

This research was primarily supported by NSF through the University of Pennsylvania Materials Research Science and Engineering Center (MRSEC) (DMR-1720530), including its Rheology, Optical and Electron Microscopy Shared Experimental Facilities. We thank the Penn Nanoscale Characterization Facility and the Laboratory for Research on the Structure of Matter (LRSM) Computational Facility. Partial support is acknowledged from NSF grants DMR-1107642 (R.W.C.), DMR-1305199 (D.J.D.), DMR-160738 (A.G.Y.), DMREF-1628407 (Z.F.), CMMI-1724519 (D.S.G.), and INSPIRE/EAR-134428 (D.J.J.); the LRSM Research Experience for Undergraduates program (E.M.); Simons Foundation grant 327939 (A.J.L.); NASA grant NNX08OOG (A.G.Y.); and Agence Nationale de la Recherche grant ANR0110NS09-01 through the Materials World Network program. N.C.K. and P.E.A. acknowledge the donors of the American Chemical Society Petroleum Research Fund (ACS-PRF-53948-ND9) for partial support. Z.F. acknowledges P. J. Walsh (Penn Chemistry) and students E. Salami-Ranjbaran and K. Cheng for tris(naphthyl)benzene (TNB) synthesis. The authors declare that they have no competing financial interests.

SUPPLEMENTARY MATERIALS

www.sciencemag.org/content/358/6366/1033/suppl/DC1
Materials and Methods
Figs. S1 to S12
Tables S1 to S3
Movies S1 and S2
References (*46*–*99*)

25 August 2016; resubmitted 15 March 2017
Accepted 18 October 2017
10.1126/science.aai8830

Science

Structure-property relationships from universal signatures of plasticity in disordered solids

E. D. Cubuk, R. J. S. Ivancic, S. S. Schoenholz, D. J. Strickland, A. Basu, Z. S. Davidson, J. Fontaine, J. L. Hor, Y.-R. Huang, Y. Jiang, N. C. Keim, K. D. Koshigan, J. A. Lefever, T. Liu, X.-G. Ma, D. J. Magagnosc, E. Morrow, C. P. Ortiz, J. M. Rieser, A. Shavit, T. Still, Y. Xu, Y. Zhang, K. N. Nordstrom, P. E. Arratia, R. W. Carpick, D. J. Durian, Z. Fakhraai, D. J. Jerolmack, Daeyeon Lee, Ju Li, R. Riggleman, K. T. Turner, A. G. Yodh, D. S. Gianola and Andrea J. Liu

Science **358** (6366), 1033-1037.
DOI: 10.1126/science.aai8830

Behavioral universality across size scales

Glassy materials are characterized by a lack of long-range order, whether at the atomic level or at much larger length scales. But to what extent is their commonality in the behavior retained at these different scales? Cubuk *et al.* used experiments and simulations to show universality across seven orders of magnitude in length. Particle rearrangements in such systems are mediated by defects that are on the order of a few particle diameters. These rearrangements correlate with the material's softness and yielding behavior.

Science, this issue p. 1033

www.sciencemag.org/content/358/6366/1033/suppl/DC1

Supplementary Materials for

Structure-property relationships from universal signatures of plasticity in disordered solids

E. D. Cubuk, R. J. S. Ivancic, S. S. Schoenholz, D. J. Strickland, A. Basu, Z. S. Davidson, J. Fontaine, J. L. Hor, Y.-R. Huang, Y. Jiang, N. C. Keim, K. D. Koshigan, J. A. Lefever, T. Liu, X.-G. Ma, D. J. Magagnosc, E. Morrow, C. P. Ortiz, J. M. Rieser, A. Shavit, T. Still, Y. Xu, Y. Zhang, K. N. Nordstrom, P. E. Arratia, R. W. Carpick, D. J. Durian, Z. Fakhraai, D. J. Jerolmack, Daeyeon Lee, Ju Li, R. Riggleman, K. T. Turner, A. G. Yodh, D. S. Gianola,* Andrea J. Liu*

*Corresponding author. Email: ajliu@physics.upenn.edu (A.J.L.); gianola@engr.ucsb.edu (D.S.G.)

Published 24 November 2017, *Science* **358**, 1033 (2017)
DOI: 10.1126/science.aai8830

This PDF file includes:

Other supplementary material for this manuscript includes the following:

Movies S1 and S2

Contents

Materials and Methods

Calculating Softness

To construct softness, we need to be able to track the positions of particles with time. We characterize the local structure around particle k using a set of M structure functions. These structure functions fall into two families,

$$G(k;\mu) = \sum_i \mathrm{e}^{(r_{ik}-\mu)^2/L^2} \tag{1}$$

$$\Psi(k;\xi,\lambda,\zeta) = \sum_{i,j} \mathrm{e}^{\left(r_{ik}^2+r_{jk}^2+r_{ij}^2\right)/\xi^2} \left(1+\lambda\cos\theta_{kij}\right)^\zeta \tag{2}$$

where μ, ξ, λ, and ζ are variables that characterize the members of each family of functions; r_{ik} is the distance between particles i and k; θ_{kij} is the angle made between particles k, i, and j. The first set of structure functions provides information about the radial density at distance μ from particle k. We choose the range of μ and ξ to be $[0, 3.5d]$, where d is the typical distance separating neighboring particles, unless we specify otherwise. The parameter L is the size of the window in radius; a delta function would correspond to the limit $L \to 0$. We choose $L = 0.1d$; this is a fine enough scale to distinguish between local variations of structure, but coarse enough so that the noise does not overwhelm the signal. The second set counts the number of large and small bond angles within a distance ξ of particle k. Here, varying $\lambda = \pm 1$ determines whether we are counting large or small bond angles. Changing ζ controls the angular resolution of the structure functions.

We assigned each structure function an orthogonal direction in M-dimensional space. The particle's local structural environment at time t, as encoded by the structure functions, is therefore represented by a point in M-dimensional space; the vector connecting the origin to this point is $\boldsymbol{F_k(t)}$. We then "train" as follows. From the experiment or simulation, we choose a small set of N_r rearranging particles and N_n particles that are not rearranging. We determine whether or not particles are rearranging as follows. For systems under mechanical load, particles with D^2_{min} above a threshold value, $D^2_{\text{min},0}$ are considered to be rearranging. In quiescent systems in which no mechanical load is applied, we also characterize rearrangements using the quantity p_{hop}. To construct p_{hop} for a particle i at time t, we first define two intervals in time, $A = [t-\delta t/2, t]$ and $B = [t, t+\delta t/2]$ and then write,

$$p_{\text{hop}}(i,t) = \sqrt{\langle(\boldsymbol{r}_i(t) - \langle\boldsymbol{r}_i(t)\rangle_B)^2\rangle_A \langle(\boldsymbol{r}_i(t) - \langle\boldsymbol{r}_i(t)\rangle_A)^2\rangle_B}. \tag{3}$$

where $\langle\cdot\rangle_A$ and $\langle\cdot\rangle_B$ are expectation values over the A and B intervals respectively, and δt is a timescale commensurate with the timescale for particles to rearrange (*29*). For quiescent systems p_{hop} offers a more sensitive measure of rearrangements that refers to single particles as opposed to neighborhoods of particles. Particles with p_{hop} above a threshold value of $p_{\text{hop},0}$ are considered to be rearranging.

We calculate the structure functions for each particle in the training set to obtain the position of each particle in M-dimensional structure-function space. We then use the method of support vector machines (SVM) to calculate the hyperplane that best separates points corresponding to rearranging particles from points corresponding to non-rearranging particles. The SVM algorithm was implemented using either the scikit-learn package (*46*) or LIBSVM package (*47*). Once the hyperplane is constructed, it can be used to classify the structural environments of particles that are not included in the training set. For each particle k, the softness S_k is defined as the signed distance of the particle's position in M-dimensional structure-function space to the hyperplane, with positive softness corresponding to particles that lie on the same side of the hyperplane as rearranging particles in the training set. The higher the softness, the more likely the particle is to rearrange (*19*).

The hyperplane encodes the relation between structure and dynamics in the system. Softness is the linear combination of the M structure functions that correlates most strongly with rearrangement dynamics. Structure functions with larger projections onto the normal to the hyperplane contribute more to softness. For systems with different interactions, the hyperplane is different and therefore the physical interpretation of

softness is different. The method is highly accurate; for systems ranging from BKS silica to Lennard-Jones glasses, oligomer glasses, experimental colloidal packings and granular packings, 75%-95% of the rearrangements occur at particles that are on the positive softness side of the hyperplane. See movies S1 and S2 for experimental and simulated systems with particles colored by both softness and D^2_{min}.

Measuring Yield Strain

For all systems in which we have measured macroscopic stress-strain curves or force-displacement data, we calculate the yield strain. We convert force and displacement data to equivalent stress and strain quantities. For the case of uniaxial experiments, we define the yield strength from the stress vs. strain response as either the clear deviation from linearity during the initial loading, or as the stress at which system-spanning shear bands forms. For instrumented indentation experiments, we use the Oliver-Pharr method (*48*) to deduce a hardness value, from which a yield strength can be estimated using an appropriate Tabor factor and values of reported Poisson's Ratio. Elastic moduli are measured from either loading or unloading curves, and are converted to an equivalent Young's modulus for comparison across systems.

ξ_r Parameter Selection

To ensure that we find the rearrangement length scale in a consistent way from system to system, we have studied how R_c^D and Δt affect ξ_r. The sampling radius, R_c^D, determines the size of the volume over which D^2_{min} is computed. In order for D^2_{min} to be well defined, we must take R_c^D to be greater than the first peak in the radial distribution function. Fig. S1A demonstrates that R_c^D has little effect on the rearrangement length scale between the first and second peaks of the radial distribution function. As the second peak is crossed, the correlation length modestly increases. To maintain consistency in our results, we report ξ_r at $R_c^D = 1.5d$ in all of the systems we study.

The second parameter, Δt, denotes the lag-time between frames. Fig. S1B illustrates how ξ_r varies with Δt. At small Δt, ξ_r is large and decreases with increasing Δt. At some finite lag-time, ξ_r begins to increase again as rearrangements induce nearby rearrangements. Thus, this minimum value of ξ_r is a good measure of the size of a single rearrangement. We report this value in all of the systems we study. For reference, the Δt which corresponds to the minimum ξ_r is typically several times longer than the ballistic timescales in molecular dynamics simulations.

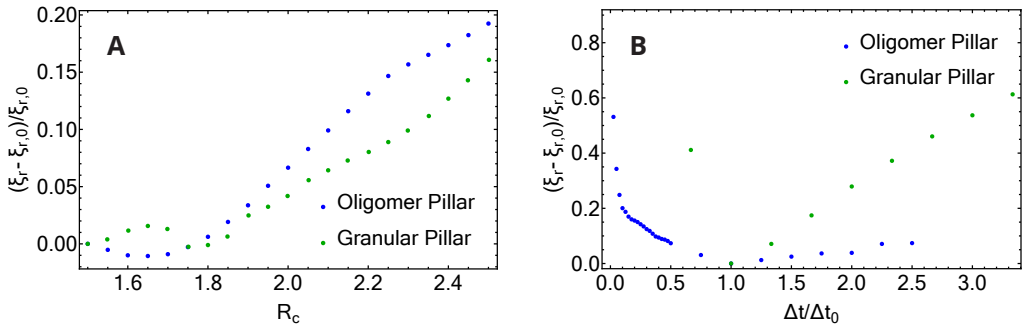

Figure S1: Demonstrates how the rearrangement length scale, ξ_r, varies with **(A)** R_c^D in units of d and **(B)** Δt. To calculate ξ_r, we fit $\exp(-r/\xi_r)$ to the spatial correlations in the D^2_{min} field at each parameter selection. These correlations are defined by Eq. 2 in the main text. Here, r is the radial distance from particles, $\xi_{r,0}$ is the reported rearrangement length scale, and Δt_0 is lag-time of the minimum ξ_r.

Amorphous Carbon Experiments

Synthesis of Carbon Films

Two sets of amorphous carbon thin films were prepared: amorphous hydrogenated carbon thin films in their regular form (a-C:H) and with silicon and oxygen dopants (a-C:H:Si:O). The a-C:H set contained two films; their growth, composition, mechanical, and tribological properties have been reported previously (*49, 50*). These two coatings were deposited by plasma-assisted chemical vapor deposition (PACVD). In a vacuum vessel, precursor gases are introduced through a shower head facing the substrates, and a DC bias voltage is applied on the cathode that holds the substrates (while the vessel is grounded), leading to the generation of a plasma. The interactions between this plasma and the substrates' surfaces will allow either etching or growth of a thin film, depending on the nature and pressure of the precursor gas and the bias voltage applied. For these films, (100) monocrystalline silicon wafers were used, the precursor gas was acetylene, at a flow of 10 sccm. For the two samples referred to as AC8 and AC5, growth was conducted at a constant pressure of 100 and 200 mTorr respectively, and an applied bias voltage of -800 and -500 V respectively. The AC5 and AC8 films were estimated to contain approximately 40 and 34 at.% H respectively (the remainder being carbon), and have 65% and 70% of the carbon atoms in the sp2-hybridization respectively, with most of the rest in the sp^3-hybridization (*49*).

The a-C:H:Si:O material is of interest due to its enhanced thermal stability compared to a-C:H (*51–53*). The growth, composition, mechanical, and tribological properties specific form used here is described in detail elsewhere (*51, 52*). Briefly, the coatings were deposited on silicon wafers by Sulzer-Metco Inc. (Winterthur, Switzerland) using a proprietary plasma-enhanced chemical vapor deposition (PECVD) process (*52, 53*). The plasma is formed from a siloxane precursor using a hot filament, and the resulting ions are deposited onto Si (100) substrates with a negative bias applied to a thickness of approximately 2 μm. The films were estimated to contain approximately 57 ± 3 at.% C; 3 ± 1 at.% O; 6 ± 1 at.% Si; and 34 ± 3 at.% H (*54*). They were determined to have 48 ± 2% of the carbon atoms in the sp^2-hybridization, with most of the rest in the sp^3-hybridization (*55*).

Mechanical Response to Nanoindentation

Unlike metallic glasses, amorphous carbons are highly covalently (directionally) bonded and tend to fail through perfect brittle fracture without evidence of shear bands or rearrangements leading to even small amounts of ductility. However, nanoindentation provides the opportunity to apply high shear stresses in the presence of significant hydrostatic compressive pressure, thus suppressing fracture. We found, consistent with previous literature studies (*56*), that plastic indents can be readily formed. While this observation for a-C:H films is not new in and of itself, the studies here were conducted with particular attention to avoiding substrate effects which can occur when the films are not sufficiently thick. Here, films were at least 10 times thicker than the maximum indentation depth.

Nanoindentation tests to obtain reduced modulus and hardness were performed using a MTS Nano Indenter XP following the continuous stiffness measurement (CSM) method described previously (*56*) while using a Berkovich tip. During the test, the load was applied exponentially versus time, in order to keep a constant strain rate throughout indentation. The ratio of the loading rate to the load (P'/P) was set at 0.03 s^{-1}. Experiments were performed in ambient air, at room temperature. The reported values of the mechanical properties include 8 or 9 distinct measurements at different locations on each sample (we were able to check the location of each indent on the surface, thanks to an integrated optical microscope).

The reduced modulus and hardness were determined for each individual indent by averaging the quantities from each individual stiffness measurement within the depth range 100–200 nm. This range was chosen to avoid both surface and substrate effects. The standard deviation of each of these quantities over the selected depth range was taken to be the experimental uncertainty. For a suitably stiff diamond probe, the Young's modulus can be determined from the reduced modulus as $E = E_{reduced}(1 - \nu^2)$, and the Poisson's ratio was determined using a surface force apparatus to be within the range $0.1 \leq \nu \leq 0.2$ (*57*). Additionally, the yield stress was determined from the hardness as $\sigma_y = H/K$, where the Tabor parameter was assumed to be in

the range $1.5 \leq K \leq 3.0$. The uncertainty expressed in the error bars is a combination of the experimental uncertainty and the uncertainty due to the conversion factors ν and K.

Metallic Glass Experiments

Synthesis of Metallic Glass Films

DC magnetron sputtering was employed to deposit $Pd_{77.5}Cu_6Si_{16.5}$ from an alloy target (*58*). The target was produced by ACI Alloys Inc. from elemental sources with 99.99% (Pd source) and 99.999% (Cu and Si source) purity. Sputter deposition was performed in an ATC Orion series magnetron sputter deposition system (AJA International Inc.). Following evacuation of the chamber to base pressures of $<5\times10^{-8}$ Torr, an argon plasma was struck at a working pressure of 4 mTorr and a target power of 125 W. Thin films were deposited simultaneously on Si [100] and soda-lime glass slides.

To control glass structural state, thin films were deposited at varying substrate temperatures. The substrate was radiatively heated using a quartz lamp heater. The substrate temperature was monitored by a shielded thermocouple, which measured heat radiated back from the sample holder. To calibrate the true temperature of the substrate, irreversible temperature sensitive dots (Omega Label) where placed on the sample holder and observed while increasing the heater set point. Therefore, all reported substrate temperatures indicate the true deposition temperature and not the heater set point.

The composition was primarily determined by energy dispersive X-ray spectroscopy (EDS) in a FEI Quanta 600 FEG Mark II using a EDAX Octane Super silicon drift detector. All spectra were taken at 5 kV and an incidence angle of 30° to ensure the electron interaction volume was fully contained by the thin film. The resulting spectra were analyzed using EDAX TEAM software suite.

To cross-validate the EDS analysis, metallic glass (MG) thin films deposited under similar conditions were analyzed using Rutherford backscatter spectroscopy (RBS). RBS spectra were collected using a NEC Mini-Tandem accelerator operating at 2 MeV. The RBS detector was calibrated using a spectrum taken from a Pb-doped aluminum oxide. The RBS spectra were analyzed using xRump and SimNRA analysis packages. The average film composition is $Pd_{78.3}Cu_{6.2}Si_{15.5}$, which agrees well with the target compositions of $Pd_{77.5}Cu_6Si_{16.5}$.

The structure of the thin films was observed through x-ray diffraction (XRD). A Rigaku Smartlab diffractometer was operated in a parallel beam geometry to collect $\theta-2\theta$ scans from 30 to 60 2θ from thin films deposited on soda-lime glass. To support the XRD analysis, FIB lift-outs were prepared from select deposition conditions. The lift-outs were observed in a JEOL 2100 transmission electron microscope operating in both bright and dark field conditions. Selected area electron diffraction patterns were also taken from within the thin film. Structural characterizations reveals consistent amorphous structures in the MG thin films.

Mechanical Response to Nanoindentation

The mechanical properties of the sputtered MG thin films were assessed by nanoindentation. An Agilent (now Keysight Technologies) G200 with XP module and diamond Berkovich tip was used to indent the thin films at a constant loading-rate-to-load-ratio (P'/P) of 0.05 s^{-1}. Depth resolved hardness and modulus of MG thin films deposited on Si substrates were determined by the continuous stiffness method. Due to the small modulus difference ($\sim$10%) between the MG films and Si, the substrate has a limited effect on the Oliver-Pharr modulus and hardness for indentation depths smaller than 25% of the film thickness (*59, 60*)

Metallic Glass Simulations

	ρ (g/cm^3)	E (GPa)	B (GPa)	μ (GPa)	ν	$2\tau_r/E$ (%)	$2\tau_{glue}/E$ (%)
Binary LJ System	1.2	39	60	15	0.36	~ 4.5	2.4
$Cu_{40}Ag_{60}$	9.6	39	85	12	0.44	~ 3.3	2.1
$Cu_{46}Zr_{54}$	6.9	38	89	12	0.44	~ 3.9	2.6
$Zr_{52.5}Cu_{17.9}Ni_{14.6}Al_{10}Ti_5$	7.0	71	153	27	0.42	~ 5.2	2.9

Table S1: Properties of metallic glasses calculated by finite-T molecular dynamics

Simulation Protocol

Metallic glasses (MGs) are simulated at the atomic scale with either pairwise interatomic potentials (*61, 62*) or embedded atom (EAM) potentials (*63–66*). Table S1 lists the density ρ, Young's modulus E, bulk modulus B, shear modulus μ, Poisson's ratio ν, the initiation shear stress τ_r and propagation shear stress τ_{glue} of a shear band in a binary Lennard-Jones (LJ) MG, two EAM binary MGs, and a 5-component EAM MG, respectively. To convert the shear stress to uniaxial tensile/compressive stress, one needs to divide by the Schmid factor of 0.5, so $2\tau_{glue}$ is the uniaxial stress to keep a 45º inclined metallic shear band in propagation once it is nucleated, and this is the value that should be compared directly to the experimental yield strength. $2\tau_{glue}/E$ (last column of Table S1) is therefore the non-dimensionalized uniaxial yield strength, that is compared across different materials.

Molecular dynamics simulations reveal that as shear transformation zones (STZ) aggregate into an embryonic shear band, and later into a mature shear band which resembles a mode-II or mode-III shear crack, the glassy material inside undergoes aged-rejuvenation-glue-liquid (ARGL) transformations (*61, 64*). The external mechanical energy input can also drive diffusive mixing (*66*) and crystallization of the processed material. At mesoscale, such hierarchical self-organization of flow defects and shear banding can also be modelled by a stochastic kinetic Monte Carlo (kMC) model (*67, 68*).

Kob-Andersen Binary Lennard-Jones Mixture Simulations

Simulation Protocol

Quiescent simulations of the Kob-Andersen (KA) mixture were performed above the dynamical glass transition. The KA mixture is a long studied fragile glass-former with Lennard-Jones interactions and no directional bonding (*31*). A detailed methodology of these simulations can be found in Refs. (*19, 20*). For completeness, we have repeated the details of the model below. We study a 10,000 particle Kob-Andersen mixture at number density $\rho = 1.20$. This model consists of an 80:20 mixture of particles interacting through the Lennard-Jones (LJ) potential with parameters: $\sigma_{AA} = 1.0$, $\sigma_{AB} = 0.8$, $\sigma_{BB} = 0.88$, $\epsilon_{AA} = 1.0$, $\epsilon_{AB} = 1.5$, $\epsilon_{BB} = 0.5$, $m_A = m_B = 1.0$. We measure distances in units of σ_{AA} and times in units of $\tau = \sqrt{m_A \sigma_{AA}^2/\epsilon_{AA}}$ with a Boltzmann constant $k_B = 1.0$. To improve the computational efficiency we cut the LJ potential off at $2.5\sigma_{AA}$ and smoothed the potential so that its second derivative is continuous at the cutoff. This mixture has been extensively characterized and features a mode-coupling temperature at $T_{MCT} \approx 0.42$. We simulate the system using LAMMPS (*69*) in an NVT ensemble using a Nosé-Hoover thermostat with a timestep of 0.0025τ. Typically, we output the state of the system every t_x and quench the states to their closest inherent structure using a combination of FIRE and conjugate gradient algorithms. This allows us to identify rearrangements with less ambiguity. Here, t_x was chosen to be a timescale that is commensurate with the crossover between ballistic and caged dynamics in the respective systems.

Microscopic Structure and Dynamics

The quiescent nature of these simulations implies that there is no large affine background motion that must be accounted for when identifying rearrangements; this should be contrasted with other systems in this study that are below their dynamical glass transition where rearrangements must be initiated by an external mechanical perturbation. In the absence of large affine deformation there is no obvious benefit of using D^2_{min} to identify rearrangements. Moreover, since D^2_{min} uses a region of size R_c^D to identify the background affine motion, it cannot identify individual particles that rearrange as well as a metric that involves only a single particle.

In quiescent systems, we therefore use a "hop" indicator function, $p_{\text{hop}}(i,t)$, as described by Eq. 3. In instances where the central particle has not rearranged we note that p_{hop} will fluctuate at the scale of the variance in particle positions during the quench. When a rearrangement occurs, p_{hop} will of order Λ^2 where $\mathbf{\Lambda}$ is the displacement of the mean position of the particle during the rearrangement. This provides a substantial separation of scales between rearranging and caged dynamics. Typically, we define a threshold of $p_{\text{hop}} \approx 0.05$ to separate these two regimes.

To construct the training set, we first must identify local environments that are most and least susceptible to rearrangement. For the former, we take a set of $N_r = 6000$ particles that will rearrange within 2τ with $p_{\text{hop}} \geq p_{\text{hop},0} = 0.6$. To identify prototypical non-rearranging particles, we identify a set of $N_n = 6000$ particles that do not rearrange for a substantial fraction of the relaxation time, τ_α. We then use a Support Vector Machine (SVM) to construct a hyperplane with a cross-validation accuracy of approximately 90%. In Fig. S2A, we draw a snapshot of the system with the particles colored according to their softness. We calculate the spatial correlation for D^2_{min} and softness. Although p_{hop} better characterizes rearrangements for a quiescent system, D^2_{min} offers a similar characterization and can be used on mechanically driven systems. Thus, to maintain a consistent definition of the rearrangement length scale (ξ_r) across quiescent and mechanically driven systems, we examine the decay length of the D^2_{min} correlation function for all systems in this study. Both the D^2_{min} and softness correlation functions are plotted in Fig. S2B and show clearly exponential correlations. We find $\xi_r = 1.08$ and $\xi_S = 1.3$.

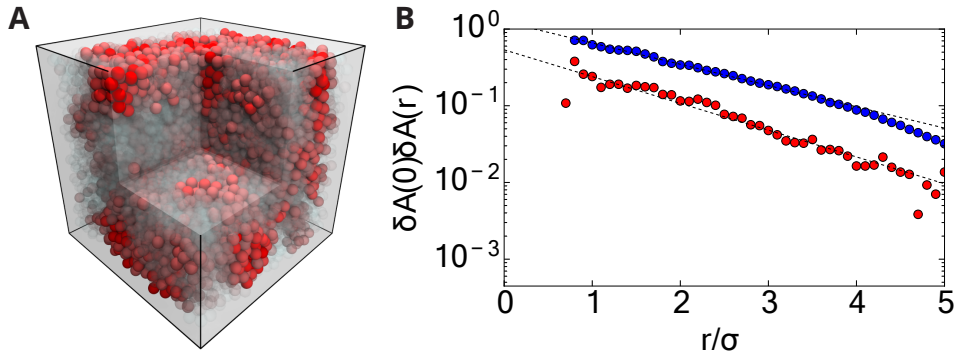

Figure S2: **(A)** A snapshot of the KA system. Particles with $S > 0$ are colored red while particles with $S < 0$ are semitransparent. Clear spatial correlations exist. **(B)** The correlation of operators $\langle \delta A(r) \delta A(0) \rangle$ for D^2_{min} (red) and S (blue).

BKS Silica Simulations

Simulation Protocol

Quiescent simulations of the van Beest, Krame and van Santen (BKS) silica (*30*) were carried out at temperatures above the dynamical glass transition. BKS silica mimics silica, the prototypical strong glass former, and features strong covalent directional bonds. It has been used to describe properties of silica melt (*70*) and amorphous silica (*71*). To prevent atoms from fusing together, which is a well known unphysical property

of the BKS potential, we have used a harmonic potential at small distances (*71*). This modification does not affect the potential at intermediate and low temperatures, but reliably prevents unphysical fusion events. We use a unit cell of 960 silicon atoms and 1920 oxygen atoms. Simulations were done using LAMMPS (*69*). We first melt α-quartz at 6000 K, and then quench it to 2500 K with a cooling rate of 5×10^{12} K s^{-1}. Data is collected using the NVT ensemble at 2500 K. We output states every 400 fs, and quench them to their inherent structure using a combination of FIRE and conjugate gradient algorithms.

Microscopic Structure and Dynamics

The hyperplane used to generate the softness field for this system was obtained using a similar method to the Kob-Anderson quiescent simulations. For completeness, we repeat the details below. Due to the quiescent nature of this simulation, we use the "hop" indicator function, $p_{\text{hop}}(i,t)$, as described by Eq. 3 for the same reasons described in the Kob-Anderson simulation section. To construct the training set, we identify local environments that are most and least susceptible to rearrangement. For the former, we take particles that will rearrange within 2τ with $p_{\text{hop}} \geq p_{\text{hop},0} = 0.6$. To identify prototypical non-rearranging particles we identify local structures that do not rearrange for a substantial fraction of the relaxation time, τ_α. With these criteria in mind, we identify $N_r = 6000$ candidates for rearranging particles and $N_n = 6000$ candidates for non-rearranging particles. The M-dimensional structure function space used to describe the local neighborhoods of silicon and oxygen atoms were described by the same radial and angular structure functions used for the Kob-Anderson quiescent simulations. We used a Support Vector Machine (SVM) to construct a hyperplane with a cross-validation accuracy of approximately 86%. The optimal C parameter of the linear SVM was found to be 1 by cross-validation. A snapshot of the system is shown in Fig. S3A. Furthermore, D^2_{min} was calculated with a cutoff of 3.75 Å. The spatial correlation functions are plotted in Fig. S3B. As with the Kob-Anderson simulations, the decay length of the D^2_{min} correlation function is found to maintain a consistant definition of the rearrangement length scale, ξ_r, across both quiescent and mechanically driven systems. Both softness and D^2_{min} have spatially exponential correlations as far as 11 Å. We find $\xi_S = 3.19$ Å and $\xi_r = 3.26$ Å. In units of the Si-Si bond length (3.1 Å), these lengths scales are $\xi_S = 1.03$ and $\xi_r = 1.05$.

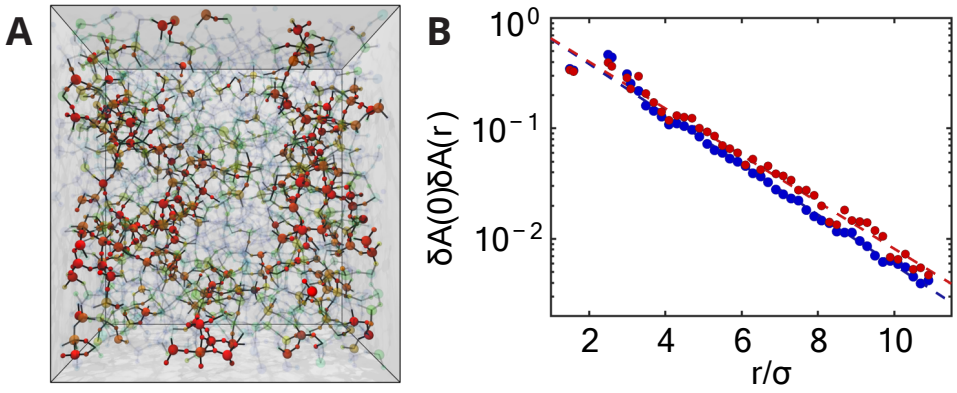

Figure S3: **(A)** A snapshot of the SiO_2 system. Particles with $S > 0$ are colored red while particles with $S < 0$ are semitransparent. Spatial correlations are apparent in this system, too. **(B)** The correlation of operators $\langle \delta A(r) \delta A(0) \rangle$ for D^2_{min} (red) and S (blue).

Oligomer Pillar Simulations

Simulation Protocol

We performed and analyzed molecular dynamics simulations of a coarse-grained model of a polymer pillar. The protocol for generating this pillar has been described in depth in prior work (*32*), but the potential has

been modified so the samples exhibit brittle failure at low temperatures. Our simulations consist of 2×10^6 monomers that are bound in chains of length 5. The bonded interactions are taken through a harmonic bonding potential,

$$U_{ij}^b = \frac{k_h}{2} \left(r_{ij} - d\right)^2, \tag{4}$$

where r_{ij} is the radial distance between monomers i and j and $k_h = 2000\epsilon/d^2$. The non-bonded interactions are taken using a modified 12-6 Lennard-Jones (LJ) potential,

$$U_{ij}^{nb} = 4\epsilon \left[\left(\frac{\sigma}{r_{ij} - \Delta} \right)^{12} - \left(\frac{\sigma}{r_{ij} - \Delta} \right)^{6} \right]. \tag{5}$$

We chose $\Delta = 0.75d$ and $\sigma = d - \Delta/2^{1/6}$ where d is the unit of length of our simulation. This gives the potential shorter range and higher curvature while restricting the minimum to reside a the same location as the standard LJ potential. We present the following results in reduced units, i.e., distance is measured in units of d, temperature is measured in units of k_h/ϵ and time is in units of $\tau = \sqrt{\epsilon/md^2}$ where m represents the mass of a single particle. This study was completed using LAMMPS (*69*) with a simulation timestep of 0.0006636τ. We analyzed pillars at 7 different temperatures, $T = 0.05$, 0.1, 0.15, 0.2, 0.25, 0.275, 0.3 and 0.325. These temperatures are all below the glass transition temperature, $T_g = 0.38 \pm 0.02$ which was found using a cooling rate of 1×10^{-7}.

We confined the polymer glasses to a pillar geometry with a diameter of $50d$ to ensure the centers of the pillars obtained "bulk-like" dynamics. The initial configuration of the pillars was found by by inserting chains which followed an ideal random walk in cylindrical space, and overlapping monomers were relaxed using a soft pushoff technique. All systems were equilibrated in the *NVT* ensemble at $T > T_g$, and equilibration continued until the monomers has diffused several times the end-to-end distance of the oligomers. Periodic boundary conditions were taken to be in the axial direction of the pillar.

Microscopic Structure and Dynamics

We quantified rearrangement of particle i between times t and $t + \Delta t$ using D^2_{min} from Eq. 1 in the main text. A particle at time t is said to be rearranging if $D^2_{\text{min}} > D^2_{min,0}$. Here we chose $D^2_{\text{min},0} = 0.1d^2$. This value was chosen by using the same method as in Ref. (*18*).

To characterize the local structure around particle i, we use a set of $M = 165$ structure functions, defined in Eqs. 1 and 2. The summations are performed for all particles within a radius R_c^S. Our results are insensitive to changes in R_c^S so long as we include the first few neighboring shells (*18*). In this work, we set $R_c^S = 2.5d$ and fixed $L = 0.05d$.

Shear bands form in many of the pillars at large strains. These shear bands contain many particles with $D^2_{\text{min}} > D^2_{\text{min},0}$. To ensure that our training set did not simply distinguish between particles in the shear band and out of the shear band, we confined ourselves to the first few timesteps of the simulation before any shear banding had occurred. Because the relaxation times differ between the exterior and interior of the pillars (*32*), we confined ourselves to the interior of the pillar, a cylinder of diameter $16d$. At each temperature, we chose $N_r = 700$ randomly from the set of rearranging particles, and $N_n = 700$ particles with the lowest values of D^2_{min} averaged over τ_α timesteps as non-rearranging particles (*19*). In each pillar, τ_α was chosen to be the relaxation time of the interior of the pillar. As in Ref. (*72*), these relaxation times were calculated by fitting the intermediate scattering function of the interior of the pillar to a KWW-stretched exponential where τ_α was chosen to be at where the function crossed 0.2, and q was chosen to be the location of the first peak in the static structure function.

It is not possible to specify a hyperplane that completely separates rearranging particles from non-rearranging ones. Thus, the SVM is designed to penalize particles whose classification is incorrect. This misclassification penalty is controlled by the parameter C where larger C values correspond to fewer incorrect classifications. This parameter was chosen to be $C = 0.1$ by nested cross validation (*73*). For this value of C, we find that more than 93% of rearrangements occur at particles with softness $S > 0$. This prediction accuracy is very

high, and is close to that obtained in Ref. (*19*). Fig. S4A-C contains snapshots of the pillar's softness field at several frames of the simulation. We calculate the spatial correlations in the softness and D^2_{min} prior to shear band formation. The correlations are clear and exponentially decay as shown in Fig. S5A-B. We find $\xi_S = 0.6d$ and $\xi_r = 0.73d$.

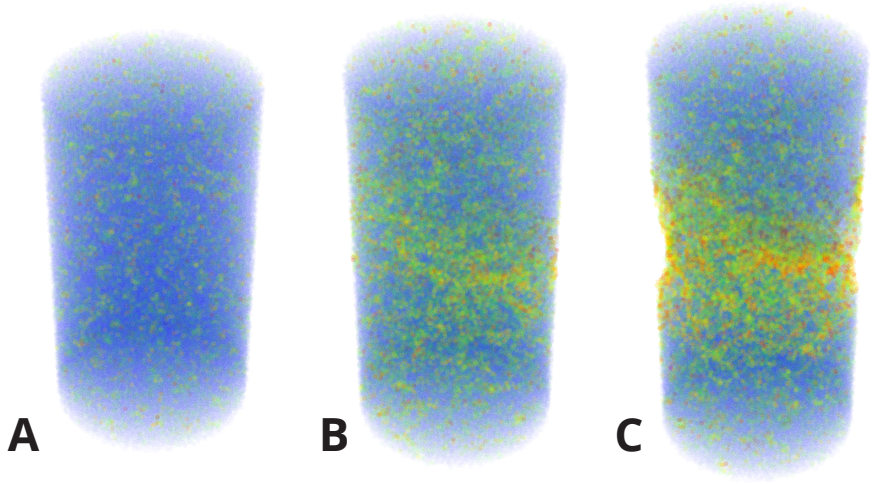

Figure S4: Plots of the softness fields of the $T = 0.2$ oligomer pillar at times **(A)** $t = 1$, **(B)** $t = 50$, and **(C)** $t = 110$. An exterior layer of particles of thickness R_c^S are removed from the graphics because their structure will be distinctly different than the bulk sample that we trained on. Softness values are on a hyperbolic tangent scale going from transparent to opaque and from blue, to green, to yellow, to orange, and finally to red. As necking develops, particles with high softness cluster around the deformation.

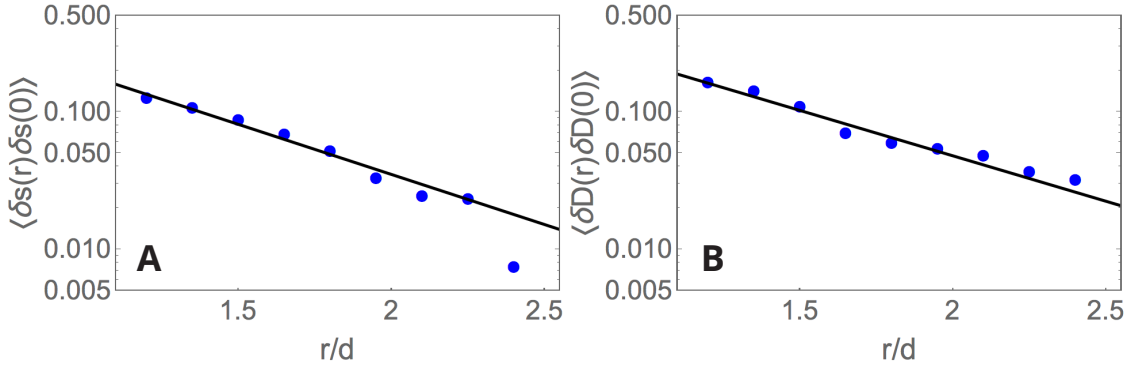

Figure S5: Normalized plots of the spatial correlations of the interior of the $T = 0.2$ pillar for **(A)** S and **(B)** D^2_{min}. The exponential decay of these correlations are clear.

Mechanical Response to Tension Applied Along Pillar Axis

To obtain the elastic moduli and yield stress for this study, we ran simulations with a standard Lennard-Jones potential between non-bonded monomers, i.e. where $\Delta = 0$ in Eq. 5. The details of these simulations have been previously described (*32*), but pertinent details are repeated below. Particles were confined to pillars about the periodic z-axis. All pillars were given an aspect ratio of 2. We varied the diameters, D, and chain lengths, N, of these pillars systematically as shown in Table S2. To strain the pillars, we lengthened the z-direction of the simulation box at two true strain rates, $\dot{\epsilon} = 3.5 \times 10^{-4}$ and $\dot{\epsilon} = 3.5 \times 10^{-5}$. These rates have been labeled the "fast" and "slow" strain rates in Table S2 respectively. We calculated stress-strain curves of each pillar directly from the LAMMPS output. The Young's Modulus, E, of each pillar was calculated by fitting a line to the stress-strain measurements before a strain of 2.2%. The yield stress, σ_y, was found by taking to be the the maximum stress of the simulation. Table S2 reports the averaged Young's Modulus and yield stress of three independent pillar configurations where the errors represent the standard error between the configurations.

N	D (nm)	$\dot{\epsilon}$	E (GPa)	δE (GPa)	σ_y (GPa)	$\delta\sigma_y$ (GPa)
5	52	slow	0.629	0.004	0.0232	0.0003
5	30	fast	0.494	0.004	0.0169	0.0004
5	30	slow	0.649	0.009	0.0234	0.0006
5	15	slow	0.67	0.07	0.026	0.002
50	30	slow	0.688	0.002	0.0246	0.0003
500	30	slow	0.70	0.01	0.0254	0.0008

Table S2: Properties of Polymer Pillar simulations

Molecular Glass Experiments

Molecular Glass Film Synthesis

All molecular glass films used for nano-indentation measurements were prepared using physical vapor deposition (PVD) in an ultra-high vacuum chamber with a base pressure of $\sim 10^{-7}$ torr. The details of the custom chamber are described in our earlier publications (*74*). Silicon (one side polished, 100 plates from Virginia Semiconductor) with 1$\sim$2 nm native oxide layer was used as the substrates for all films. Small organic molecule N,N$^{'}$-Bis(3-methylphenyl)-N,N$^{'}$-diphenylbenzidine (TPD) was purchased from Sigma-Aldrich and used without further purification. 1,3-bis(1-naphthyl)-5-(2-naphthyl)benzene was synthesized by palladium catalyzed suzuki cross-coupling of 1-bromo-3-chloro-5-iodobenzene with naphthylboronic acids. The details of the synthesis is reported in our earlier publications (*74, 75*). Mixture of TPD and TNB powder were premelted in vacuum oven to ensure full mixing before vapor deposition. For TPD films, the substrate temperature was held at 341 K ($T_{g,TPD}$ + 13 K). For TNB films, the substrate temperature was held at 291K ($T_{g,TNB}$ - 52 K). The as-deposited films were annealed in a vacuum oven at 363K ($T_{g,TNB}$ + 20 K) for 20 minutes before the indentation measurements to ensure that the as-deposited glass is transformed into an ordinary liquid-quenched glass (*74*). For TPD+TNB mixture films, the substrate temperature was held at 353 K ($T_{g,TPD}$ + 25 K or $T_{g,TNB}$ + 10 K). An average deposition rate of 0.5 - 1 nm/s was used for all films. An in-situ quartz crystal micro-balance (QCM) was used to monitor film thickness during deposition. After deposition of roughly 1 μm films, the substrate temperature was brought back to room temperature before the sample was removed from the chamber.

Mechanical Response to Nanoindentation

Indentation experiments were performed using a diamond Berkovich tip in a Hysitron TI-950® nanoindenter. Prior to the indentation tests on the molecular glass films, the area function of the Berkovich tip was calibrated. Indentation tests into a fused silica sample, with known Young's modulus and hardness, were done at a range

of loads to yield measurements at different contact depths. The area function was then determined by fitting a model, assuming a known Young's modulus and hardness of the fused silica, to the measurements.

Indentation tests on the molecular glass films (TPD, TNB, TPD+TNB) were performed in load control. For each test, the load was ramped up to the peak load in 5 s, held for 2 s and then unloaded over 5 s. Indents were performed at seven different peak loads between 50 μN and 200 μN. Measurements were performed at 5 randomly selected locations for each load on each specimen, thus the reported values represent the average of 35 measurements for each specimen. The force-displacement (FD) curves were recorded at a rate of 200 Hz. The reduced Young's modulus and hardness were obtained by analyzing the FD curves using the Oliver-Pharr method (*76*). The yield strength was estimated as $1/3$ of the measured hardness.

Nanoparticle Film Experiments

Nanoparticle Film Synthesis

Packings of silica nanoparticles (d = 20.0 $\pm$ 4.8 nm) with thin alumina coatings were spin-coated on to silicon wafers from aqueous solutions to produce films between 100 and 500 nm thick. This rapid deposition technique, along with the polydispersity, ensured that the film was amorphous. Ellipsometry confirmed that the packing fraction was close to random close packing.

Mechanical Response to Nanoindentation

Nanoindentation performed using atomic force microscopy was used to measure the mechanical response of the films. The advantage of using nanoparticles is that, unlike in atomic systems, loads can be applied and localized to *single constituent particles*. The cantilever probes were stiff silicon probes, with the tips coated with diamond-like carbon for robustness. These probes were also used to image the topography of the film in tapping mode both before and after indentations were performed, as shown in Fig. S6A. The high-resolution topography images were correlated and subtracted to produce an image of the changes in the film, revealing the motions of particles resulting from the applied stress as shown in Fig. S6B. The plastically-affected region is only a single particle in size in this example, and is seldom more than three particles (*i.e.*, a few tens of nanometers across), indicating that this technique probes particle-level deformation mechanisms without producing a shear band or an avalanche of rearrangement events.

Maximum loads in a range between 100 and 800 nN were applied, and each indent was performed at a unique site at least 100 nm from its nearest neighbors to avoid interference. Data from the force curves (example in Fig. S6C) were used to extract an effective (reduced) modulus using the methods of (*48*). Established methods for evaluating hardness were also employed. Considerable local variations in mechanical properties were found, demonstrating that the film is structurally inhomogeneous. For more details, see (*77*).

The Young's modulus was estimated from the effective modulus based on reasonable estimates of the Poisson's ratio (Poisson's ratio is uncertain in a disordered packing, and likely varies spatially due to differences in local density and structure). Tabor's relation, by which the yield stress is calculated from the hardness, is also inexact (*78*); mathematically, this has a much greater effect on the computed yield stress than Poisson's ratio. We conservatively assumed Tabor's ratio to range from 2 to 4.5, leading to the uncertainty depicted as error bars in Fig. S6D. Nevertheless, the hardness and yield stress exhibit a positive correlation, as indicated by the dotted line representing a yield strain of 0.044. This relationship is in good agreement with that found from the other systems discussed elsewhere in this paper.

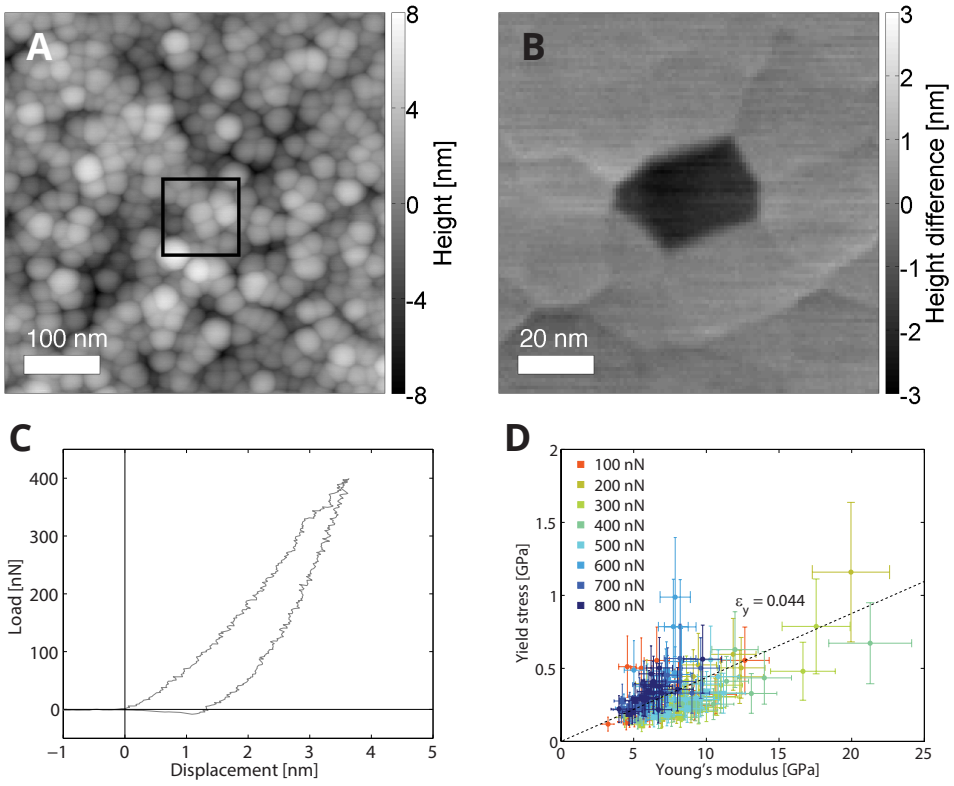

Figure S6: **(A)** An example topography scan from before indents were performed, and **(B)** the difference image comparing the before scan with its after scan. The region is the black rectangle in **(A)**, showing that the plastically deformed region is only a single nanoparticle in size. **(C)** An example force curve from which mechanical properties were extracted, and **(D)** the relationship between yield stress and modulus for this experiment. The significant uncertainty, discussed in the text, is evident. Squares represent the data from a 500 nm thick film, while circles represent the data from a 100 nm thick film. Figs. **(A,B,C)** adapted with permission from (*77*). Copyright 2016 American Chemical Society.

2D PNIPAM Colloid Experiments

PNIPAM Colloid Packing Synthesis

The experimental system is made of soft poly(N-isopropyl acrylamide) (PNIPAM) microgel particles synthesized by surfactant-free radical emulsion polymerization (*79*). PNIPAM becomes more hydrophobic at higher temperature (> 32 °C), and hence the microgel particle diameter decreases when sample temperature is raised. As a result, the particle diameter and thus sample volume fraction can be tuned by controlling suspension temperature. In this experiment we use bidisperse mixture of PNIPAM spheres with two different sizes $d = 1.4$ μm and $d = 1.1$ μm (at 24 °C). A quasi-2D packing is prepared by sandwiching a small amount (0.6 μL) of solution containing bidisperse PNIPAM spheres between two 18×18 mm^2 glass cover slips (Thermo Fisher Scientific). Fig. S7A provides a schematic of the sample cell and microscope setup. The sample thickness is set to be similar to the diameter of the large particles. To prevent the solvent from evaporating, the sandwiched cell is sealed peripherally by optical glue (Norland 65) which is subsequently cured with light from a UV lamp for 30 minutes.

Before measurement, the sample cell is left to relax/age at room temperature for two days. This step is necessary, in large part because it helps reduce drift inside the sample. The sample cell is then transferred

onto a glass slide and placed on the sample stage of a Leica DMRB upright microscope. We use a $100\times$ oil immersion objective (NA=1.4) and an extra 1.25x internal magnification for imaging. An objective heater (Bioptechs) is employed to control sample temperature in-situ over a range from room temperature to 40 °C with 0.1 °C step resolution. During the present experiments the sample temperature is set at 28 °C wherein the packing fraction of PNIPAM spheres is slightly below the jamming point; this choice of packing fraction insures that a sufficient number of rearrangement events occurs for the analysis.

Fig. S7B is a micrograph of the bidisperse PNIPAM colloidal sample. Over the full field-of-view, the sample contains approximately 3600 large particles and 3400 small particles. Inset: An enlarged image of a smaller area within the sample which shows that the two species of large and small particles are well mixed, i.e., crystallization is not observed. Since PNIPAM hydrogel can deform under compression, their spherical diameters are not well-defined in a near jammed condition. Instead we derive effective diameters, $d_0 \simeq 1.2$ μm and $d_1 \simeq 0.9$ μm for large and small particles, respectively, by using the position of the first peak in the radial distribution function, $g(r)$. The effective diameter is thus utilized as an indicator of particle size. Using this effective diameter we calculate an effective packing fraction of $\phi \simeq 85\%$. A CCD camera (UP-900DS-CL, UNIQVision) captures images of the sample; it is coupled to the host computer, and video capture software XCAP (EPIX) is employed for data acquisition, etc. The recorded video frames have a spatial resolution of 1392×1036 pixels and 256 gray scales. Video is recorded at a frame rate of 10 fps for 6 hours. In total, 180,000 video frames are generated. An open-source particle-tracking software trackpy (*80*) is used to extract particle trajectories. With the current imaging parameters we estimate a tracking accuracy of approximately 10 nm.

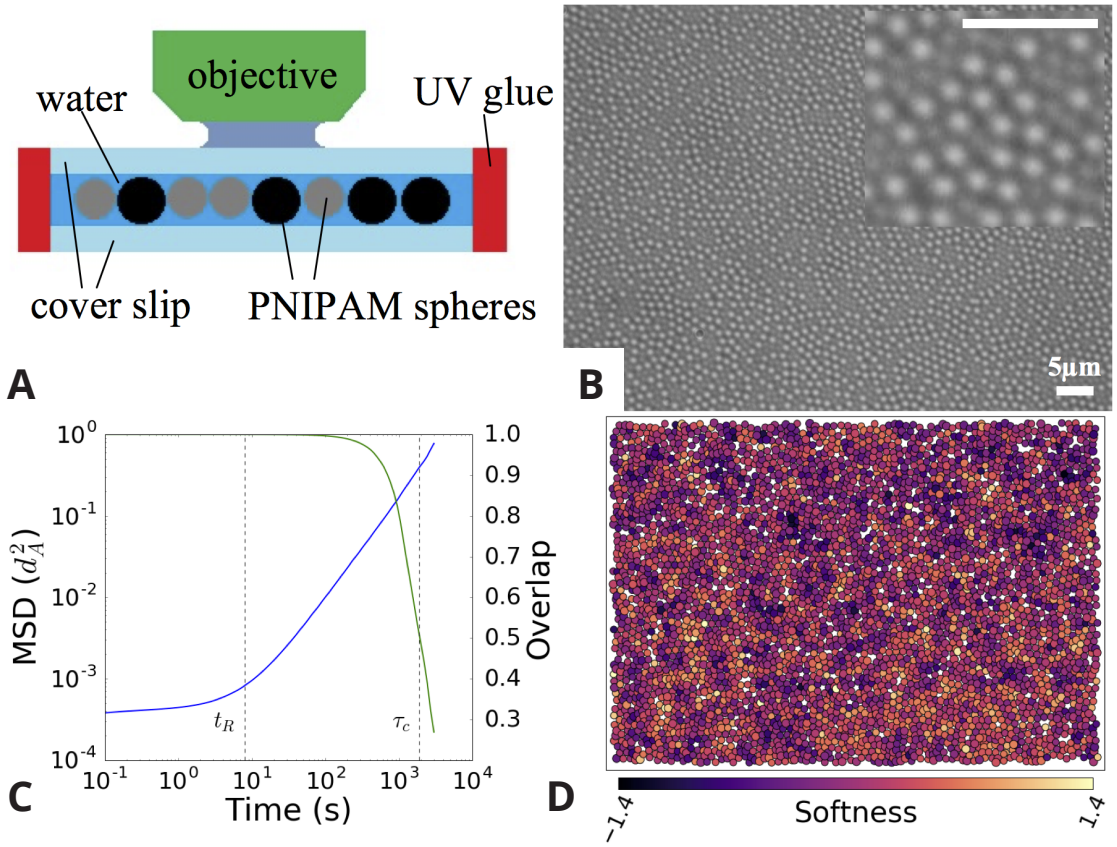

Figure S7: **(A)** Schematic of experimental setup. The PNIPAM microgel particle suspension is sandwiched by two cover slips (light blue) which in turn are sealed by UV glue (red). **(B)** Micrograph of quasi-2D bidisperse PNIPAM colloidal glass. Inset: A zoom-in view of a smaller area within the sample. The scale bars in both images are 5 μm. **(C)** Mean square displacement (blue) data derived from one-sixth of the entire experiment and the corresponding overlap function for that time period (green). Approximately 6 alpha relaxation periods occur during the entire experiment. **(D)** Exemplary frame of the softness field computed for both particle species.

Microscopic Structure and Dynamics

As with the other quiescent systems in this study, the "hop" indicator function, p_{hop}, as described by Eq. 3, was used to correlate local structure with dynamics for the reasons laid out in the Kob-Anderson simulations section. The rearrangement timescale, δt, is chosen to be longer than the particle's caging timescale so that large values in p_{hop} reflect cage breaking dynamics (*19*). In the present case, we chose δt to be 8 seconds. This timescale is the lag time wherein the plateau in the measured mean square displacement ends Fig. S7C. The following analysis is based on large particles which are easier to track and provide enough rearrangement events for the analysis. A particle i is said to be rearranging at time t, if $p_{\text{hop}}(i,t) > p_{\text{hop},0}$. The threshold $p_{\text{hop},0} = 0.1$ is chosen to maximize cross validation scores in the final step. Similarly, a particle i is said to be stable, if p_{hop} remains below a low threshold of 0.005 for at least τ_c. This threshold is chosen to be larger than typical cage fluctuations but much smaller than $p_{\text{hop},0}$. The stability time, τ_c, is the time at which the self-overlap function first falls below 0.5, as seen in Fig. S7C (*19*).

We characterized the local structure of particle i with a set of 94 structure functions, defined in Eqs. 1

and 2. The calculations are performed for all particles within a radius $R_c^S = 5.0\ d_0$ (*18*). For rearranging particles, the structure is computed at a time Δt before the particle's p_{hop} increased above the lower threshold. For stable particles, structure functions are computed at the start of the stability period τ_c. Note, our results are insensitive to changes in R_c^S provided that we include the first few neighboring shells (*18*). Particles within a distance R_c^S from the boundary of the field of view are not included in the analysis.

We use all rearranging particles in the training set, and an equal number of stable particles are randomly selected from those particles that do not cross the lower threshold (*19*). We find a cross-validation accuracy of $72\% \pm 3\%$ using these training samples, and the training score is approximately 75% for both rearranging and stable particle classes. For a constant number of training samples, higher training scores are possible using more restrictive p_{hop} thresholds, but this gain is at the expense of lower cross-validation scores. This observation suggests that our prediction accuracy is currently limited by the small number of rearrangement events observed in our experimental time frame. Fig. S7D shows the softness field computed for both particle species. Note, the cross-validation accuracy for small particles is only 62%.

Rearrangements can also be quantified by the non-affine structural changes experienced by particle i at time t; this characterization procedure uses D^2_{min} from Eq. 1 in the main text. As with the Kob-Anderson and BKS simulations, we examine the decay length of the D^2_{min} correlation function to maintain a consistent definition of rearrangement length scale, ξ_r, across the quiescent and mechanically driven systems in this study. The correlations of the D^2_{min} scalar field are shown next to the correlations of the softness scalar field, S, in Fig. S8. We find $\xi_r = 0.87$ and $\xi_S = 1.09$.

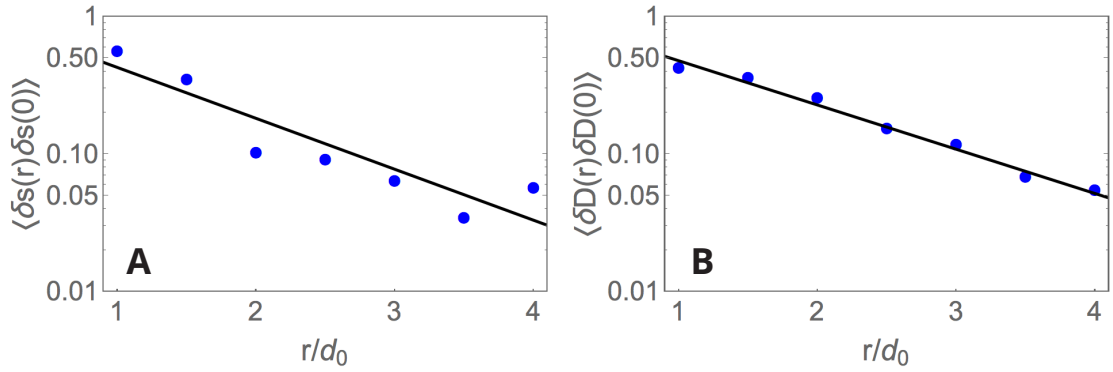

Figure S8: Normalized plots of the spatial correlations for **(A)** S and **(B)** D^2_{min}.

3D PNIPAM Colloid Experiments

PNIPAM Suspension Synthesis

The shear rheology of dense aqueous suspensions of colloidal N-isopropylacrylamide (NIPA) gel particles was measured by both a novel microfluidic technique (*81*) as well as with a conventional rheometer (*82*). These particles are soft, and they swell with temperatures; therefore, the volume fraction may be tuned across the jamming transition by varying the temperature of a single sample.

Macroscopic Mechanical Response

Above jamming, the stress versus strain rate flow curve can be fit to a Herschel-Bulkley form in order to extrapolate to zero strain rate for an estimate of the yield stress, which we interpret as the strength; see Fig. 3 of Ref. (*81*) and Fig. 2 of Ref. (*82*). The corresponding shear moduli are found from $G'(\omega)$ rheometry data, as in Fig. 5 of Ref. (*82*), by extrapolating to $\omega = 0$. The resulting data points in the strength versus modulus plot are for both monodisperse and bidisperse samples of different size particles.

Colloid Pillar Experiments

Colloid Pillar Synthesis

Pillars for macroscopic mechanical measurements were synthesized by filling capillary tubes (inner diameter = 580 μm) with a suspension of $d = 3.00$ and $d = 6.15$ μm diameter polystyrene (PS) spheres in volume ratio $V_L/V_S = 3.78$, where V_L and V_S are the total volumes of the 6.15 μm and 3.00 μm particles, respectively. The bidisperse mixture is chosen to suppress crystallization; optical and electron microscopies are used to confirm an amorphous packing.

After allowing the suspension of colloidal particles to dry, two wires are inserted into both ends of the capillary tube and a piezoelectric actuator is brought into contact with one of the wires. The opposite wire is coupled to a load cell, enabling measurement of the axial force. Sinusoidal displacements are produced by the actuator, which remains in contact with the wire. The displacement periodically loads and unloads the pillar about the mean confining force, resulting in a gradual densification of the pillar and an increase in the packing fraction, ϕ. The average packing fraction of the confined pillar is determined using high-resolution optical microscopy and microbalance measurements.

Microscopic Structure and Dynamics

Experimental systems for microscopic particle measurements were created by injecting a suspension of fluorescent $d = 3.3$ μm poly(methyl methacrylate) (PMMA) particles into a reservoir. The reservoir was constructed such that one wall was movable, which allows for the packing to be deformed. Polydispersity in the particle size of between 6% and 8% leads to an amorphous packing. The top of the reservoir was sealed using a thin piece of coverglass to allow for imaging using a laser-scanning confocal microscope. Because the PMMA particles and CXB have the same index of refraction, micrographs can be collected deep into the specimen.

The deformation experiment proceeded by displacing the movable wall using a piezoelectric actuator and then collecting a sequence of micrographs of the packing that were then assembled into a volume. The volumes imaged were always tens of particle diameters away from any walls to minimize the effects of boundaries. Typical displacement increments were 0.6 μm ($\approx 0.2d$). The total deformation profile imposed was a sine wave with increasing amplitude from one cycle to the next. A computer algorithm was used to identify the centers of particles in each 3D volume with uncertainty in the particle positions of $\approx 0.03d$. After particle centers were identified, the positions at each timestep were linked into trajectories that spanned the duration of the compression experiment.

To quantify rearrangement of particle i between times t and $t + \Delta t$, we calculated D^2_{min} from Eq. 1 in the main text. A particle at time t is said to be rearranging if $D^2_{\text{min}} > D^2_{\text{min},0}$. Here, we chose $D^2_{\text{min},0} = 0.075d^2$. Because the imposed deformation was not uniform between timesteps, the incremental strain also varied non-uniformly between timesteps. To place the times t and $t + \Delta t$ on equal footing, we constructed an artificial box near the boundaries of the imaging volume. From one timestep to the next, we map the deformation of the box using the displacements of particles within a small distance of the planes that define the box's faces. We then use the displacements of the box's corners to find the displacement gradient tensor, $\mathbf{J}$, and the macroscopic strain tensor $\boldsymbol{\epsilon} = \frac{1}{2}\left(\mathbf{J^T J} - \mathbf{I}\right)$. We calculate the shear (deviatoric) invariant,

$$\eta^s = \sqrt{\frac{1}{2} Tr\left(\boldsymbol{\epsilon} - \epsilon^m \mathbf{I}\right)^2}, \tag{6}$$

of the system between timestep t and each subsequent timestep t'. Here, $\epsilon^m = \frac{1}{3} Tr\boldsymbol{\epsilon}$ is the hydrostatic strain invariant. Then, for each timestep t, we chose Δt so that the shear invariant of the system was greater than a threshold, $\eta^s > \eta^s_0$. In this case, we chose our threshold to be $\eta^s_0 = 0.04$.

We characterized the local structure around particle i with a set of $M = 157$ structure functions, defined in Eqs. 2 and 3. The summations are performed for all particles within a radius R^S_c (*18*). Our results are insensitive to changes in R^S_c so long as we include the first few neighboring shells (*18*). In this work, we set $R^S_c = 2.5d$ and fixed $L = 0.05d$.

It was found that particles with diameters less than $0.95d$ were significantly more mobile than larger particles. To ensure that our SVM really classified rearrangements and not simply large and small particles, we excluded these particles from our training set. Because particles near the boundary of the imaged volume have fewer neighbors than particles in the interior, the structure functions in these two regions differ. This difference could throw off our training. Thus, we also excluded particles less than $2.5d$ from the boundary from our training set. To construct our training set, we then chose all $N_r = 739$ rearranging particles in our system, and $N_n = 739$ particles from $t = 20$ with the lowest cumulative D^2_{min} over $\tau = 76$ timesteps, 78% of the length of the experiment, as non-rearranging particles (*19*). Typically, τ is chosen to be on the order of the relaxation time of the system, but because so few particles rearranged in this experiment, τ was chosen to be large with respect to the length of the experiment but also to avoid the aging regime near the beginning of the experiment. This value of τ is more than 10 times the average lag time, Δt, chosen for the instantaneous D^2_{min} calculations used to determine rearrangements.

It is not possible to specify a hyperplane that completely separates rearranging particles from non-rearranging ones. Thus, the SVM is designed to penalize particles whose classification is incorrect. This misclassification penalty is controlled by the parameter C where larger C values correspond to fewer incorrect classifications. This parameter was chosen to be $C = 1.0$ by nested cross validation (*73*). For this value of C, we find that 77% of rearrangements occur at particles with softness $S > 0$. Spatial correlations in the D^2_{min} and softness fields decay exponentially as shown in Fig. S9A-B. We find $\xi_S = 1.12d$ and $\xi_r = 1.03d$ respectively.

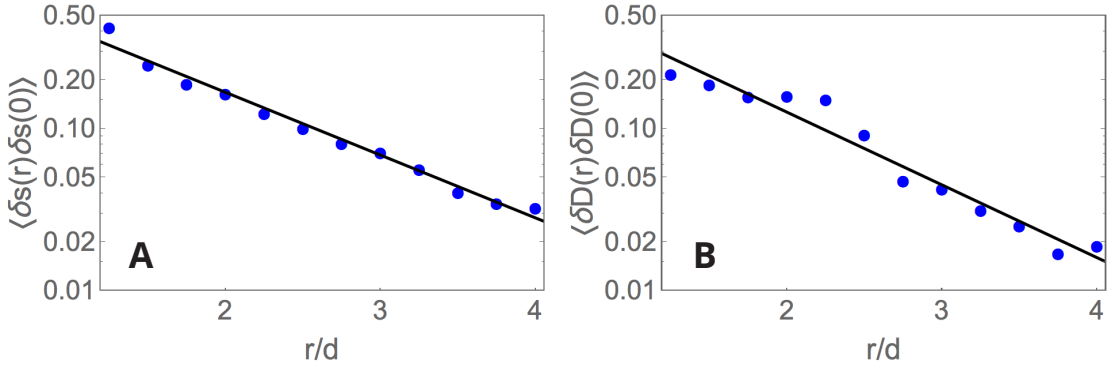

Figure S9: Normalized plots of the spatial correlations more than $2.5d$ from the boundary for **(A)** S and **(B)** D^2_{min}. These figures clearly demonstrate the exponential decay in these fields.

Macroscopic Mechanical Response to Pillar Compression

After annealing, the capillary is secured to a grip attached to the load cell. A groove machined in the grip ensures axial alignment of the capillary and the load cell axis. The pillars are made free-standing by extruding a desired length l_o from the capillary and the compression experiment proceeds by displacing a silicon punch secured to the piezoelectric actuator into the face of the pillar. The actuator is driven at a constant displacement rate between 0.1 and 1 μm $/s$ to a specified maximum displacement. Reflectance confocal micrographs acquired during compression are used to determine the displacement of the punch and the base of the pillar, thereby allowing axial strain, $\Delta l/l_o$, within the pillar to be calculated. Our experimental setup is contained within an environmental chamber, enabling control of the relative humidity (RH) during testing. RH can alter the stiffness of a single pillar, which we attribute to variations in the amount of water contained within the pillar structure, affecting the number and connectivity of capillary bridges that form between particles (and thus the cohesive interactions).

We define the ultimate compressive strength of the pillars as the maximum normalized force, $F_{max}/A_o \equiv \sigma_{max}$ (A_o is the cross sectional area of the undeformed pillar), sustained by a pillar during a compression

cycle. We also define an effective elastic modulus upon loading, E_{load}, based on a linear fit to F/A_o vs. $\Delta l/l_o$ between initial loading and the first yielding event. The yield strain is determined by the ratio of the ultimate compressive strength to the loading modulus, $\epsilon_y = \sigma_{max}/E_{load}$. For more details, see (*41, 83*).

Colloidal Monolayer Shear Experiments

Colloidal Monolayer Synthesis

The interfacial material (i.e. colloidal monolayer) investigated here consists of bidisperse (50% by number) mixture of $d = 4.1$ μm and $d = 5.6$ μm sulfate latex particles (Invitrogen) adsorbed at the interface between water and oil (decane); see Fig. S10A. These particles have dipole-dipole repulsion and so form a stable rigid monolayer even though particles never touch.

Macroscopic Mechanical Response

A custom-made interfacial stress rheometer (ISR) (*84–86*) is used to investigate the dynamics of particle rearrangements and rheology of dense particle suspensions adsorbed at a flat oil-water interface. This device allows for the visualization of the fluid microstructure (i.e. particles) while simultaneously measuring the suspension's oscillatory rheology (e.g. G'', G'). As shown in Fig. S10B, a magnetized needle is placed on the interface to be studied, between two walls. Electromagnets move the needle back and forth, shearing the interface between the needle and the walls. Monitoring the position of the needle allows inference of mechanical properties of the interface, making the device a sensitive stress-controlled shear rheometer.

The walls of the ISR are 18 mm long and spaced 3.5 mm apart. The steel needle has length 24 mm and diameter 0.23 mm. The needle experiences a restoring force from pair of Helmholtz coils, which have a maximum field at the center of the device. Time-varying force is applied with an additional computer-controlled coil. The equation of motion for the needle position is given by $m\ddot{x} = AI_{drive} - kx - d\dot{x} - F_S$, where m is the needle mass, I_{drive} is the current in the computer-controlled coil, k is the spring constant for the Helmholtz field, d represents drag from the bulk fluid, and F_S is due to any material adsorbed at the surface. If m is known, the values of k, d, and A may be determined by applying a sinusoidal I_{drive} with a clean interface (i.e. no particles) at a range of frequencies, and subsequently used to measure the oscillatory rheology of a material from $x(t)$ (*84*).

In this system, particles adsorb to the walls and needle, creating a rough boundary that hinders slippage. It is important to decouple the rheology of the surface from that of the bulk fluids above and below it. This decoupling is characterized by the Boussinesq number, the dimensionless ratio of interfacial and bulk viscosities, $Bq = |\eta_i^*|/\eta_b a$, where η_i^* is the complex interfacial viscosity (in N m^{-1}s), η_b is the bulk fluid viscosity (in Pa s), and for the ISR, a is the diameter of the needle. For surface deformations (and therefore strain measurements) to accurately reflect surface rheology (*85*) requires $Bq \gg 1$. In our present experiments Bq is approximately 100, which is adequate for the measurements we report here.

To consistently prepare the material for each experiment, oscillatory forcing at large strain amplitude γ_0 is performed for 6 cycles and then stopped. All experiments are at 0.1 Hz; we have observed that rheology depends only weakly on frequency in this regime (*87*). The present model system is non-Brownian in that no thermal motion is observed, and area fraction is varied by changing the quantity of particles dispersed into the experimental cell, a 6 cm-diameter glass dish.

Fig. S10C shows the viscous and elastic moduli of a dense particle monolayer (area fraction = 43%) as a function of the strain amplitude γ_0. The data shows that the elastic modulus (G') is at least an order of magnitude larger than the viscous modulus (G''). A decrease in G' accompanied by an increase in G'' at larger values of γ correspond to a partial loss of rigidity and the onset of yielding. This loss of rigidity is also apparent by plotting the quantity tan $\delta = G''/G'$ as a function of γ_0 (Fig. S10c, inset).

For Fig. 3 of the main paper, we use the value of elastic shear modulus G' in the low-strain plateau in Fig. S10C, and convert to Young's modulus E by assuming an isotropic material with Poisson ratio 0.5, so that $E = \frac{3}{2}G'$. Both E and $\sigma_y \simeq G'\gamma_y$ are then scaled by the typical interparticle spacing of 8.1 μm to obtain 3D quantities.

One of the main advantages of the ISR is that the material microstructure can be imaged while performing rheological experiments. We image particles at the oil-water interface with a resolution of 1.1 μm/pixel, permitting the tracking of each particle in a 2 mm-long section of the channel (up to 50,000 particles) during shear. Tracking is performed using a high-speed camera, a microscope, and trackpy software (*80*). Particle tracks are analyzed to compute local strain, strain rate, and D^2_{min}. Fig. S10D shows the displacement vectors for a section of the material as it rearranges under shear.

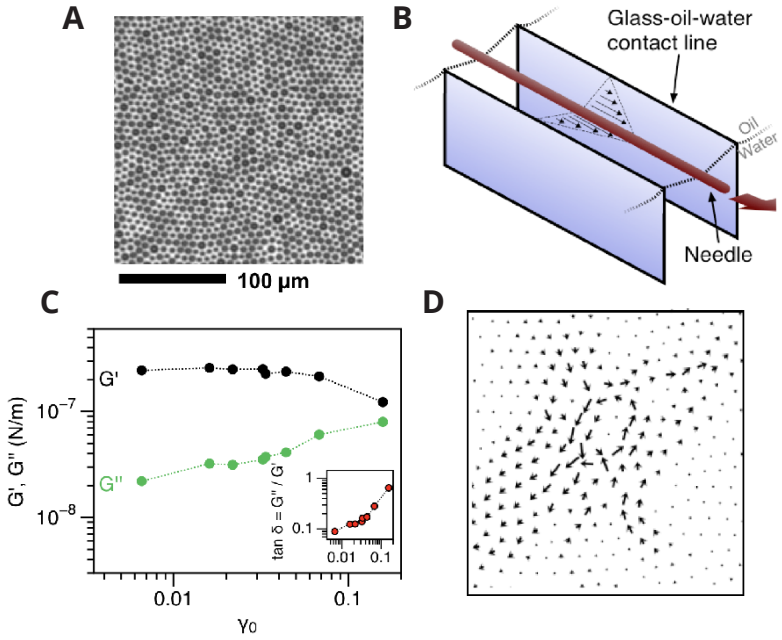

Figure S10: **(A)** Particles adsorbed at the water-oil interface viewed from above, with area fraction 43%. **(B)** Sketch of ISR apparatus: a ferromagnetic needle is embedded in the interfacial material to be measured, between two fixed walls. Magnetic forcing of the needle produces uniform shear of the film (velocity profile sketched). **(C)** Bulk rheology of the interfacial material. Response shows near-linear elasticity at small strain amplitude, but a yielding transition and loss of rigidity above $\gamma_0 \approx 0.06$. Inset: Ratio G''/G' as function of γ_0. **(D)** Displacement vectors for a set of particles after rearranging under shear.

Aqueous Foam Shear Experiments

Macroscopic Mechanical Response

The rheological behavior of a commercial foam is reported in Ref. (*88*). It consists of eight percent surfactant solution and bubble of mean size 60 μm, with a distribution that grows at fixed shape with time due to coarsening. The static shear modulus is inferred to be $G_0 = 230$ Pa, with the value set by the ratio of surface tension to bubble size. The yield strain was previously measured to be $\gamma_y = 0.05$ (*89*) based on changes in the rate of rearrangement events detected by diffusing-wave spectroscopy. This gives one point for the strength versus modulus plot, with an effective strength of $\gamma_y G_0 = 12$ Pa.

The rheology of custom-made aqueous foams is reported in Fig. 4 of Ref. (*90*) for about 25 samples with gas volume fractions ranging from about 0.7 up to nearly 1. The shear modulus is estimated from $G'(\omega)$ at $\omega = 1$ rad/s at low amplitudes, and the yield strain is estimated from behavior versus amplitude. As gas volume fraction increases across the range of samples, the yield strain increases from 0.06 to 0.18, and the shear modulus increases from 33 to 170 Pa.

Granular Pillar Compression Experiments

Granular Pillar Synthesis

Bulk granular materials are opaque. So, in order to be able to track individual grains during an imposed deformation, a quasi-two dimensional granular system was constructed from right-circular acetal cylinders standing upright on a horizontal substrate (*18, 91–93*). A 2D granular pillar is created inside a large box, 62 cm, which sits horizontally on an optical table (see Fig. S11). Two threaded rods are affixed to the edges of this box with only the freedom to rotate. This rotation is driven by a stepper motor and results in the translational motion of an aluminum plate held by the rods. Deformation of the pillar begins when a suspended rod, which hangs from brackets mounted to the aluminum plate, is driven into the packing. Throughout the deformation, forces imposed by the driven suspended rod are measured as this rod is pushed by the packing into two force sensors mounted to the aluminum plate. In a similar setup at the static end of the pillar, a suspended rod is pushed into the two force sensors mounted to the surrounding box, allowing for the measurement of the forces transmitted through the pillar during the deformation. An LED lightbox illuminates the pillar from beneath the clear acrylic base of the box and provides uniform, constant lighting.

Grains within the pillar are cylindrical acetal dowel pins, standing upright on the base of the box so that only the tops of the grains are visible in Fig. S11. The pillars are bi-disperse with small grain diameter 4.8 mm, large grain diameter 6.4 mm, and all grain heights 19.05 mm. The grain density is $\rho = 1.4$ g/cc. The grains have masses of around 0.46 g for small grains and 0.82 g for large grains. We estimate that the coefficient of kinetic friction between the grains and the substrate is $\mu_{meas} = 0.23 \pm 0.01$ by measuring the force required to push a wedge of grains along the substrate.

To ensure similar initial conditions across experiments, pillars are manually forced to conform to the shape and size of a rigid frame. The pillar shown inside the apparatus in Fig. S11 is representative of the initial conditions created with this method. For experiments presented here, the ratio of initial pillar height, H_0, to initial width, W_0, is 2. Once a pillar has been created, the stepper motor drives the aluminum plate at a constant speed $v_c = 0.085$ mm/s. Images and force sensor readings are acquired simultaneously throughout the compression at 8 Hz.

Particle locations are determined using a custom edge-detection-based-code which identifies the center of each particle as the point which is equidistant from all edges. Particle tracks are linked together by determining the minimum distance between particle centers in consecutive time points.

Microscopic Structure and Dynamics

The following procedure for generating the softness field in these pillars has been well described in Ref. (*18*) but will be repeated here for completeness. We quantified rearrangement of particle i between times t and $t + \Delta t$ using D^2_{min} from Eq. 1 in the main text. Here, we chose $R_c^D = 1.5d$. A particle at time t is said to be rearranging if $D^2_{\text{min}} > D^2_{\text{min},0}$. Here we chose $D^2_{\text{min},0} = 0.25d^2$.

The local structure around particle i was characterized by a set of $M = 160$ structure functions, defined in Eqs. 2 and 3. The summations are performed for all particles within a radius R_c^S. Our results are insensitive to changes in R_c^S so long as we include the first few neighboring shells (*18*). Compression of the mechanical pillar affects particles above a "front" that advances toward the bottom with time. We chose $N_r = 6000$ randomly from the set of rearranging particles, and $N_n = 6000$ particles with the lowest values of D^2_{min} within this front. Particles within a horizontal slice were said to be in this front if the avaerage speed of that slice was greater than 0.04m/s.

We then used an SVM with a misclassification penalty controlled by the parameter C. Larger C values correspond to fewer incorrect classifications. Our results were insensitive to this parameter for $C > 0.1$. In this system, we find that more than 80% of rearrangements occur at particles with softness $S > 0$. Fig. 1A-B in Ref. (*18*) contains snapshots of the pillar's softness field. The correlations in softness and D^2_{min} exponentially decay as shown in the main text in Fig. 1. We find $\xi_S = 2.21$ and $\xi_r = 2.3$.

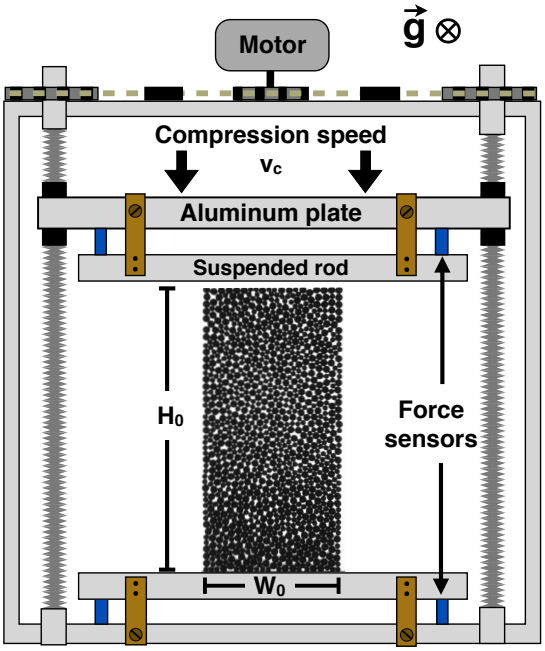

Figure S11: Top-down view of the experimental apparatus. Stepper motor rotation results in the translation of the aluminum plate, which drives the suspended rod into the disordered granular pillar at a constant speed. The pillar is 2D, allowing for visualization of all grains throughout the deformation. Images are acquired from a camera mounted above while force sensor data is simultaneously recorded from sensors mounted to the aluminum plate as well as those mounted to the side of the surrounding box.

Macroscopic Mechanical Response

The data in Fig. 4 of Ref. (*91*) show that the yield strain is about $\gamma = 0.02$ and that the 2D stress to compress the pillar is roughly constant at $12mg\mu/d$ beyond the yield strain. The corresponding 3d stress is $12mg\mu/(dh) = 165$ Pa; we interpret this as the strength. The corresponding modulus is $165/\gamma = 8250$ Pa.

Granular Bed Shear Experiments

Granular Bed Synthesis

We measure the velocity profile of a three-dimensional granular bed of 1.5 mm PMMA grains under constant shear stress applied by flow of a viscous oil driven from above the bed surface (*94, 95*). We identify the yield stress τ_c of the material at the onset of creep, which occurs at a depth Δz_c from the surface of the material. Because there are no horizontal stress gradients in this system, the yield stress is equal to applied shear stress τ_0, which we measure in the limit where it is dominated by a viscous stress $\tau_0 = \eta_f \dot{\gamma}_f$, where we control the applied fluid shear-rate $\dot{\gamma}_f$, see Fig. S12 .

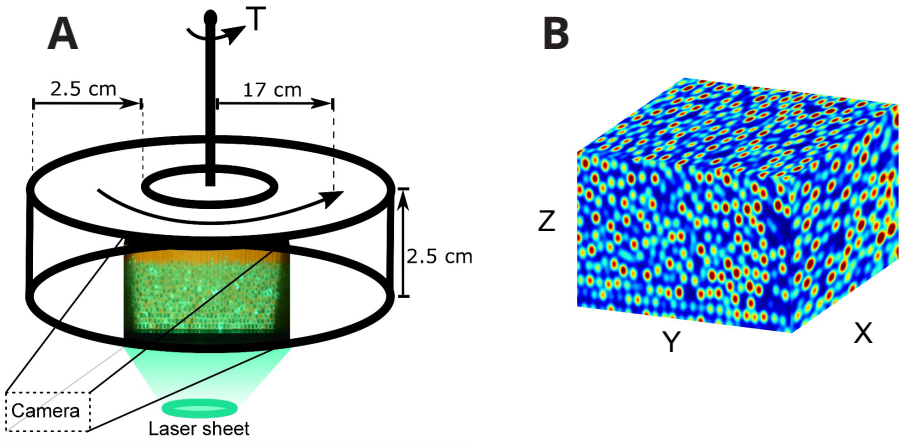

Figure S12: **(A)** Schematic of annular shear cell used to drive granular bed with a fixed fluid shear rate. **(B)** Reconstruction of positions in the granular bed obtained by refractive index matched laser scanning.

Macroscopic Mechanical Response

In our system, the confining stress is gravitational, allowing us to measure the confining pressure at the onset of creep by measuring the confining hydrostatic grain pressure. After determining the location of the yield surface from direct particle-tracking, we integrate $\frac{dP}{dz} = \Delta\rho\phi$ starting above the surface, where $\Delta\rho = (\rho_s - \rho_f)$, ρ_s is the grain density, ρ_f is the fluid density, and $\phi(z)$ is the grain packing fraction. We estimate the loading modulus by assuming the packs are near isostaticity (*96*), using the expression:

$$B = (\tilde{E}\phi_c Z)^{2/3} \left(\frac{P}{\tilde{B}}\right)^{1/3}$$

where B is the bulk modulus of the granular bed, Z is the average contact number, $\tilde{B}$ is a characteristic modulus for contacts, and ϕ_c is the packing fraction in the region of interest. This scaling of the bulk modulus has been observed in experimental and simulated systems, where the scaling exponent depends on the details of the interaction potential (*97*). Our choice of an exponent of $1/3$ is consistent with a scaling controlled by Hertzian contacts (*96*). Namely, we assume that contact forces scale as $F \propto -\delta^{3/2}$, giving the scaling $B \propto P^{1/3}$. In these experiments, the confining pressure is of Pa scale relative to the grain bulk modulus of GPa scale. In this limit of small loading, the relevant loading modulus is much softer than the grain modulus, instead being of the same scale as the confining pressure (*98*). Because grain-scale rearrangements can be achieved by forces on the scale of the gravitational weight of a single particle, we choose the characteristic scale for the modulus $\tilde{B}$ to be the gravitational confining stress of a layer of grains $\Delta\rho g d$. We also choose $Z = 6$, and $\phi_c = 0.64$, which suffices for order of magnitude analysis.

The relevant equations for an isotropic elastic medium under plane stress are $\sigma_{xy} = \tau = 2\mu\epsilon_{xy}$ and $\sigma_{yy} = P = \lambda\theta + 2\mu\epsilon_{yy}$, where $\theta = \epsilon_{xx} + \epsilon_{yy} = (\Delta\phi)/\phi_0$ is the volumetric strain giving the relative increase in volume, and μ, λ are Lamé constants. The packing fraction in our system approximately follows (*95*) the constitutive relation $\phi(I_v) = \frac{\phi_m}{1+I_v^{1/2}}$, so we can estimate the volumetric strain from measurements of $I_v = \eta_f \dot{\gamma}/P$ by using the relation $\theta = \frac{1}{2}\frac{I_v}{1+I_v^{1/2}}$. From our observations of $I_c \approx 10^{-7}$ at the onset of creep (see Fig. 3 of Ref. 94), we get an estimate of the volumetric strain of $\theta \approx 10^{-7}$. Because $\epsilon_{yy} = O(1)\theta$, we can estimate $\lambda \approx P/\theta$ in a way that is largely insensitive to the precise values of the strains ϵ_{yy} and ϵ_{xx}, and then obtain the shear moduli. We have verified our results by making direct estimates of the ratio $\epsilon_{yy}/\epsilon_{xx} \approx 1$ from instantaneous grain displacements, and find the resulting estimates of the shear moduli unchanged. Using the identities $\mu = G$ and $\lambda = K - \frac{2}{3}G$, we extract the shear modulus G consistent with the

elastic system of two equations for grains at the onset of creep. The resulting estimates of the shear modulus are of order $G = 10^6$ Pa, giving a large ratio for $G/B \approx 10^6$ for all experiments. This observation of a large G/B ratio suggests the onset of creep is very close to isostaticity based on the known scalings of G/B to distance to isostaticity (*99*). Last, we obtain an estimate of the Young's modulus using $E = \frac{9BG}{3B+G}$. The numerical values are given in Table S3.

P_c (Pa)	τ_c (Pa)	K (Pa)	G (KPa)	E (Pa)
2.97	0.80	3.65	17.8	21.9
2.09	0.59	3.25	12.6	19.5
1.11	0.34	2.64	6.67	15.8
0.66	0.24	2.22	3.96	13.3
0.71	0.22	2.27	4.26	13.6

Table S3: Measurements of confining pressure, yield stress, and loading modulus. The typical uncertainties for P_c are 0.1 Pa, for τ_c, 0.05 Pa, and the typical uncertainty for E, combining the uncertainty in the typical contact number, critical packing fraction, and measurement uncertainties is $\pm 30\%$. Note, the most significant uncertainty in the determination of E is the average contact number.

Movie S1: Oligomer Pillar Deformation

An oligomer pillar pulled in tension. Particles are colored by their non-affine displacement, D^2_{min} (left), and softness (right). Before deformation, softness is homogeneously distributed in the bulk of the pillar. As deformation proceeds, strain localizes in a band of the pillar, which is reflected in the large values of D^2_{min} in this plane. Strain localization is accompanied by an increase in the softness within the band.

Movie S2: Granular Pillar Deformation

A granular pillar deformed in compression. The pillar is formed by arranging granular rods in an amorphous packing that is confined between two plattens. The top platten moves from top to bottom and imposes deformation. Grains are colored by their non-affine displacement, D^2_{min} (left), and softness (right). During deformation, plasticity is concentrated near the platten. Chains of particles with high D^2_{min} form along directions of high shear stress, which are oriented along directions approximately 45° from the pillar axis. The plasticity near the top platten increases the softness in this region of the pillar.

References

1. M. M. Trexler, N. N. Thadhani, Mechanical properties of bulk metallic glasses. *Prog. Mater. Sci.* **55**, 759–839 (2010). doi:10.1016/j.pmatsci.2010.04.002

2. H. M. Jaeger, S. R. Nagel, R. P. Behringer, Granular solids, liquids, and gases. *Rev. Mod. Phys.* **68**, 1259–1273 (1996). doi:10.1103/RevModPhys.68.1259

3. N. P. Bansal, R. H. Doremus, *Handbook of Glass Properties* (Academic Press, 1986).

4. K. E. Parmenter, F. Milstein, Mechanical properties of silica aerogels. *J. Non-Cryst. Solids* **223**, 179–189 (1998). doi:10.1016/S0022-3093(97)00430-4

5. L. E. Nielson, R. F. Landel, *Mechanical Properties of Polymers and Composites*, vol. 2 (Marcel Dekker, 1981).

6. C. A. Schuh, T. C. Hufnagel, U. Ramamurty, Mechanical behavior of amorphous alloys. *Acta Mater.* **55**, 4067–4109 (2007). doi:10.1016/j.actamat.2007.01.052

7. M. Chen, Mechanical behavior of metallic glasses: Microscopic understanding of strength and ductility. *Annu. Rev. Mater. Res.* **38**, 445–469 (2008). doi:10.1146/annurev.matsci.38.060407.130226

8. F. Barthelat, R. Rabiei, Toughness amplification in natural composites. *J. Mech. Phys. Solids* **59**, 829–840 (2011). doi:10.1016/j.jmps.2011.01.001

9. R. O. Ritchie, The conflicts between strength and toughness. *Nat. Mater.* **10**, 817–822 (2011). doi:10.1038/nmat3115 Medline

10. J. Robertson, Diamond-like amorphous carbon. *Mater. Sci. Eng. Rep.* **37**, 129–281 (2002). doi:10.1016/S0927-796X(02)00005-0

11. J. Herrmann, K.-H. Müller, T. Reda, G. R. Baxter, B. Raguse, G. J. J. B. de Groot, R. Chai, M. Roberts, L. Wieczorek, Nanoparticle films as sensitive strain gauges. *Appl. Phys. Lett.* **91**, 183105 (2007). doi:10.1063/1.2805026

12. L. Zhang, G. Feng, Z. Zeravcic, T. Brugarolas, A. J. Liu, D. Lee, Using shape anisotropy to toughen disordered nanoparticle assemblies. *ACS Nano* **7**, 8043–8050 (2013). doi:10.1021/nn403214p Medline

13. P. C. Hiemenz, *Principles of Colloid and Surface Chemistry* (Marcel Dekker, ed. 2, 1986).

14. R. M. Nedderman, *Statics and Kinematics of Granular Materials* (Cambridge Univ. Press, 1992).

15. D. Gidaspow, *Multiphase Flow and Fluidization: Continuum and Kinetic Theory Descriptions* (Academic Press, 1994).

16. H. J. Herrmann, J. P. Hovi, S. Luding, *Physics of Dry Granular Media* (Kluwer Academic, 1998).

17. A. Greer, Y. Cheng, E. Ma, Shear bands in metallic glasses. *Mater. Sci. Eng. Rep.* **74**, 71–132 (2013). doi:10.1016/j.mser.2013.04.001

18. E. D. Cubuk, S. S. Schoenholz, J. M. Rieser, B. D. Malone, J. Rottler, D. J. Durian, E. Kaxiras, A. J. Liu, Identifying structural flow defects in disordered solids using machine-learning methods. *Phys. Rev. Lett.* **114**, 108001 (2015). doi:10.1103/PhysRevLett.114.108001 Medline

19. S. S. Schoenholz, E. D. Cubuk, D. M. Sussman, E. Kaxiras, A. J. Liu, A structural approach to relaxation in glassy liquids. *Nat. Phys.* **12**, 469–471 (2016). doi:10.1038/nphys3644

20. E. D. Cubuk, S. S. Schoenholz, E. Kaxiras, A. J. Liu, Structural properties of defects in glassy liquids. *J. Phys. Chem. B* **120**, 6139–6146 (2016). doi:10.1021/acs.jpcb.6b02144 Medline

21. S. S. Schoenholz, E. D. Cubuk, E. Kaxiras, A. J. Liu, Relationship between local structure and relaxation in out-of-equilibrium glassy systems. *Proc. Natl. Acad. Sci. U.S.A.* **114**, 263–267 (2017). doi:10.1073/pnas.1610204114 Medline

22. See supplementary materials.

23. M. L. Falk, J. S. Langer, Dynamics of viscoplastic deformation in amorphous solids. *Phys. Rev. E* **57**, 7192–7205 (1998). doi:10.1103/PhysRevE.57.7192

24. A. Argon, H. Kuo, Plastic flow in a disordered bubble raft (an analog of a metallic glass). *Mater. Sci. Eng.* **39**, 101–109 (1979). doi:10.1016/0025-5416(79)90174-5

25. D. J. Durian, D. A. Weitz, D. J. Pine, Multiple light-scattering probes of foam structure and dynamics. *Science* **252**, 686–688 (1991). doi:10.1126/science.252.5006.686 Medline

26. P. Schall, D. A. Weitz, F. Spaepen, Structural rearrangements that govern flow in colloidal glasses. *Science* **318**, 1895–1899 (2007). doi:10.1126/science.1149308 Medline

27. M. L. Falk, J. S. Langer, Deformation and failure of amorphous, solidlike materials. *Annu. Rev. Condens. Matter Phys.* **2**, 353–373 (2011). doi:10.1146/annurev-conmatphys-062910-140452

28. L. Berthier, G. Biroli, J.-P. Bouchaud, L. Cipelletti, W. van Saarloos, *Dynamical Heterogeneities in Glasses, Colloids, and Granular Media* (Oxford Univ. Press, 2011).

29. R. Candelier, A. Widmer-Cooper, J. K. Kummerfeld, O. Dauchot, G. Biroli, P. Harrowell, D. R. Reichman, Spatiotemporal hierarchy of relaxation events, dynamical heterogeneities, and structural reorganization in a supercooled liquid. *Phys. Rev. Lett.* **105**, 135702 (2010). doi:10.1103/PhysRevLett.105.135702 Medline

30. B. W. H. van Beest, G. J. Kramer, R. A. van Santen, Force fields for silicas and aluminophosphates based on *ab initio* calculations. *Phys. Rev. Lett.* **64**, 1955–1958 (1990). doi:10.1103/PhysRevLett.64.1955 Medline

31. W. Kob, H. C. Andersen, Scaling behavior in the β-relaxation regime of a supercooled Lennard-Jones mixture. *Phys. Rev. Lett.* **73**, 1376–1379 (1994). doi:10.1103/PhysRevLett.73.1376 Medline

32. A. Shavit, R. A. Riggleman, Strain localization in glassy polymers under cylindrical confinement. *Phys. Chem. Chem. Phys.* **16**, 10301–10309 (2014).

33. C. Brito, M. Wyart, Heterogeneous dynamics, marginal stability and soft modes in hard sphere glasses. *J. Stat. Mech.* **2007**, L08003 (2007). doi:10.1088/1742-5468/2007/08/L08003

34. D. J. Ashton, J. P. Garrahan, Relationship between vibrations and dynamical heterogeneity in a model glass former: Extended soft modes but local relaxation. *Eur. Phys. J. E* **30**, 303–307 (2009). doi:10.1140/epje/i2009-10531-6 Medline

35. J. Rottler, S. S. Schoenholz, A. J. Liu, Predicting plasticity with soft vibrational modes: From dislocations to glasses. *Phys. Rev. E* **89**, 042304 (2014). doi:10.1103/PhysRevE.89.042304 Medline

36. S. S. Schoenholz, A. J. Liu, R. Riggleman, J. Rottler, Understanding plastic deformation in thermal glasses from single-soft-spot dynamics. *Phys. Rev. X* **4**, 031014 (2014). doi:10.1103/PhysRevX.4.031014

37. S. Patinet, D. Vandembroucq, M. L. Falk, Connecting local yield stresses with plastic activity in amorphous solids. *Phys. Rev. Lett.* **117**, 045501 (2016). doi:10.1103/PhysRevLett.117.045501 Medline

38. D. M. Sussman, S. S. Schoenholz, E. D. Cubuk, A. J. Liu, Disconnecting structure and dynamics in glassy thin films. *Proc. Natl. Acad. Sci. U.S.A.* **114**, 10601–10605 (2017).

39. W. L. Johnson, K. Samwer, A universal criterion for plastic yielding of metallic glasses with a $(T/T_g)^{2/3}$ temperature dependence. *Phys. Rev. Lett.* **95**, 195501 (2005). doi:10.1103/PhysRevLett.95.195501 Medline

40. Y. Q. Cheng, A. J. Cao, H. W. Sheng, E. Ma, Local order influences initiation of plastic flow in metallic glass: Effects of alloy composition and sample cooling history. *Acta Mater.* **56**, 5263–5275 (2008). doi:10.1016/j.actamat.2008.07.011

41. D. J. Strickland, Y.-R. Huang, D. Lee, D. S. Gianola, Robust scaling of strength and elastic constants and universal cooperativity in disordered colloidal micropillars. *Proc. Natl. Acad. Sci. U.S.A.* **111**, 18167–18172 (2014). doi:10.1073/pnas.1413900111 Medline

42. V. V. Kozey, S. Kumar, Compression behavior of materials: Part I. Glassy polymers. *J. Mater. Res.* **9**, 2717–2726 (1994). doi:10.1557/JMR.1994.2717

43. C. Tang, L. P. Da'vila, Strain-induced structural modifications and size-effects in silica nanowires. *J. Appl. Phys.* **118**, 094302 (2015). doi:10.1063/1.4929875

44. J. T. Uhl, S. Pathak, D. Schorlemmer, X. Liu, R. Swindeman, B. A. W. Brinkman, M. LeBlanc, G. Tsekenis, N. Friedman, R. Behringer, D. Denisov, P. Schall, X. Gu, W. J. Wright, T. Hufnagel, A. Jennings, J. R. Greer, P. K. Liaw, T. Becker, G. Dresen, K. A. Dahmen, Universal quake statistics: From compressed nanocrystals to earthquakes. *Sci. Rep.* **5**, 16493 (2015). doi:10.1038/srep16493 Medline

45. D. V. Denisov, K. A. Lörincz, J. T. Uhl, K. A. Dahmen, P. Schall, Universality of slip avalanches in flowing granular matter. *Nat. Commun.* **7**, 10641 (2016). doi:10.1038/ncomms10641 Medline

46. F. Pedregosa, G. Varoquaux, A. Gramfort, V. Michel, B. Thirion, O. Grisel, M. Blondel, P. Prettenhofer, R. Weiss, V. Dubourg, J. Vanderplas, A. Passos, D. Cournapeau, M. Brucher, M. Perrot, É. Duchesnay, Scikit-learn: Machine learning in Python. *J. Mach. Learn. Res.* **12**, 2825–2830 (2011).

47. C.-C. Chang, C.-J. Lin, LIBSVM: A library for support vector machines. *ACM Trans. Intell. Syst. Technol.* **2**, 27 (2011). doi:10.1145/1961189.1961199

48. W. C. Oliver, G. M. Pharr, Measurement of hardness and elastic modulus by instrumented indentation: Advances in understanding and refinements to methodology. *J. Mater. Res.* **19**, 3–20 (2004). doi:10.1557/jmr.2004.19.1.3

49. C. Donnet, A. Grill, Friction control of diamond-like carbon coatings. *Surf. Coat. Tech.* **94–95**, 456–462 (1997). doi:10.1016/S0257-8972(97)00275-2

50. C. Donnet, J. Fontaine, F. Lefèbvre, A. Grill, V. Patel, C. Jahnes, Solid state ^{13}C and ^{1}H nuclear magnetic resonance investigations of hydrogenated amorphous carbon. *J. Appl. Phys.* **85**, 3264–3270 (1999). doi:10.1063/1.369669

51. D. Neerinck, P. Persoone, M. Sercu, A. Goel, C. Venkatraman, D. Kester, C. Halter, P. Swab, D. Bray, Diamond-like nanocomposite coatings for low-wear and low-friction applications in humid environments. *Thin Solid Films* **317**, 402–404 (1998). doi:10.1016/S0040-6090(97)00631-7

52. D. Neerinck, P. Persoone, M. Sercu, A. Goel, D. Kester, D. Bray, Diamond-like nanocomposite coatings (a-C:H/a-Si:O) for tribological applications. *Diamond Relat. Mater.* **7**, 468–471 (1998). doi:10.1016/S0925-9635(97)00201-X

53. T. W. Scharf, J. A. Ohlhausen, D. R. Tallant, S. V. Prasad, Mechanisms of friction in diamondlike nanocomposite coatings. *J. Appl. Phys.* **101**, 063521 (2007). doi:10.1063/1.2711147

54. J. Peng, A. Sergiienko, F. Mangolini, P. E. Stallworth, S. Greenbaum, R. W. Carpick, Solid state magnetic resonance investigation of the thermally-induced structural evolution of silicon oxide-doped hydrogenated amorphous carbon. *Carbon* **105**, 163–175 (2016). doi:10.1016/j.carbon.2016.04.021

55. F. Mangolini, J. Hilbert, B. J. McClimon, J. R. Lukes, R. W. Carpick, Thermally-induced structural evolution of silicon- and oxygen-containing hydrogenated amorphous carbon. arXiv:1711.00957 (2017).

56. J. Fontaine, J. L. Loubet, T. Le Mogne, A. Grill, Superlow friction of diamond-like carbon films: A relation to viscoplastic properties. *Tribol. Lett.* **17**, 709–714 (2004). doi:10.1007/s11249-004-8077-x

57. S. Bec, A. Tonck, J. Fontaine, *Philos. Mag.* **86**, 5465 (2006).

58. D. J. Magagnosc, G. Feng, L. Yu, X. Cheng, D. S. Gianola, Isochemical control over structural state and mechanical properties in Pd-based metallic glass by sputter deposition at elevated temperatures. *APL Mater.* **4**, 086104 (2016). doi:10.1063/1.4960388

59. S. Han, R. Saha, W. Nix, Determining hardness of thin films in elastically mismatched film-on-substrate systems using nanoindentation. *Acta Mater.* **54**, 1571–1581 (2006). doi:10.1016/j.actamat.2005.11.026

60. J. Hay, B. Crawford, Measuring substrate-independent modulus of thin films. *J. Mater. Res.* **26**, 727–738 (2011). doi:10.1557/jmr.2011.8

61. F. Shimizu, S. Ogata, J. Li, Yield point of metallic glass. *Acta Mater.* **54**, 4293–4298 (2006). doi:10.1016/j.actamat.2006.05.024

62. M. Wakeda, J. Saida, J. Li, S. Ogata, Controlled rejuvenation of amorphous metals with thermal processing. *Sci. Rep.* **5**, 10545 (2015). doi:10.1038/srep10545 Medline

63. Y. Wang, J. Li, A. V. Hamza, T. W. Barbee Jr., Ductile crystalline-amorphous nanolaminates. *Proc. Natl. Acad. Sci. U.S.A.* **104**, 11155–11160 (2007). doi:10.1073/pnas.0702344104 Medline

64. F. Shimizu, S. Ogata, J. Li, Theory of shear banding in metallic glasses and molecular dynamics calculations. *Mater. Trans.* **48**, 2923–2927 (2007). doi:10.2320/matertrans.MJ200769

65. C.-C. Wang, Y.-W. Mao, Z.-W. Shan, M. Dao, J. Li, J. Sun, E. Ma, S. Suresh, Real-time, high-resolution study of nanocrystallization and fatigue cracking in a cyclically strained metallic glass. *Proc. Natl. Acad. Sci. U.S.A.* **110**, 19725–19730 (2013). doi:10.1073/pnas.1320235110 Medline

66. Y. Mao, J. Li, Y.-C. Lo, X. Qian, E. Ma, Stress-driven crystallization via shear-diffusion transformations in a metallic glass at very low temperatures. *Phys. Rev. B* **91**, 214103 (2015). doi:10.1103/PhysRevB.91.214103

67. P. Zhao, J. Li, Y. Wang, Heterogeneously randomized STZ model of metallic glasses: Softening and extreme value statistics during deformation. *Int. J. Plast.* **40**, 1–22 (2013). doi:10.1016/j.ijplas.2012.06.007

68. P. Zhao, J. Li, Y. Wang, Extended defects, ideal strength and actual strengths of finite-sized metallic glasses. *Acta Mater.* **73**, 149–166 (2014). doi:10.1016/j.actamat.2014.03.068

69. S. Plimpton, Fast parallel algorithms for short-range molecular dynamics. *J. Comput. Phys.* **117**, 1–19 (1995). doi:10.1006/jcph.1995.1039

70. I. Saika-Voivod, P. H. Poole, F. Sciortino, Fragile-to-strong transition and polyamorphism in the energy landscape of liquid silica. *Nature* **412**, 514–517 (2001). doi:10.1038/35087524 Medline

71. K. Vollmayr, W. Kob, K. Binder, Cooling-rate effects in amorphous silica: A computer-simulation study. *Phys. Rev. B* **54**, 15808–15827 (1996). doi:10.1103/PhysRevB.54.15808 Medline

72. A. Shavit, R. Riggleman, Influence of backbone rigidity on nanoscale confinement effects in model glass-forming polymers. *Macromolecules* **46**, 5044–5052 (2013). doi:10.1021/ma400210w

73. G. Cawley, N. L. C. Talbot, On over-fitting in model selection and subsequent selection bias in performance evaluation. *J. Mach. Learn. Res.* **11**, 2079–2107 (2010).

74. T. Liu, K. Cheng, E. Salami-Ranjbaran, F. Gao, C. Li, X. Tong, Y.-C. Lin, Y. Zhang, W. Zhang, L. Klinge, P. J. Walsh, Z. Fakhraai, The effect of chemical structure on the stability of physical vapor deposited glasses of 1,3,5-triarylbenzene. *J. Chem. Phys.* **143**, 084506 (2015). doi:10.1063/1.4928521 Medline

75. T. Liu, K. Cheng, E. Salami-Ranjbaran, F. Gao, E. C. Glor, M. Li, P. J. Walsh, Z. Fakhraai, Synthesis and high-throughput characterization of structural analogues of molecular glassformers: 1,3,5-trisarylbenzenes. *Soft Matter* **11**, 7558–7566 (2015). doi:10.1039/C5SM01044F Medline

76. W. C. Oliver, G. M. Pharr, An improved technique for determining hardness and elastic modulus using load and displacement sensing indentation experiments. *J. Mater. Res.* **7**, 1564–1583 (1992). doi:10.1557/JMR.1992.1564

77. J. A. Lefever, T. D. B. Jacobs, Q. Tam, J. L. Hor, Y.-R. Huang, D. Lee, R. W. Carpick, Heterogeneity in the small-scale deformation behavior of disordered nanoparticle packings. *Nano Lett.* **16**, 2455–2462 (2016). doi:10.1021/acs.nanolett.5b05319 Medline

78. D. M. Marsh, Plastic flow in glass. *Proc. R. Soc. London Ser. A* **279**, 420–435 (1964). doi:10.1098/rspa.1964.0114

79. T. Still, K. Chen, A. M. Alsayed, K. B. Aptowicz, A. G. Yodh, Synthesis of micrometer-size poly(N-isopropylacrylamide) microgel particles with homogeneous crosslinker density and diameter control. *J. Colloid Interface Sci.* **405**, 96–102 (2013). doi:10.1016/j.jcis.2013.05.042 Medline

80. D. Allan *et al*. (2014); available at github.com/soft-matter/trackpy.

81. K. N. Nordstrom, E. Verneuil, P. E. Arratia, A. Basu, Z. Zhang, A. G. Yodh, J. P. Gollub, D. J. Durian, Microfluidic rheology of soft colloids above and below jamming. *Phys. Rev. Lett.* **105**, 175701 (2010). doi:10.1103/PhysRevLett.105.175701 Medline

82. A. Basu, Y. Xu, T. Still, P. E. Arratia, Z. Zhang, K. N. Nordstrom, J. M. Rieser, J. P. Gollub, D. J. Durian, A. G. Yodh, Rheology of soft colloids across the onset of rigidity: Scaling behavior, thermal, and non-thermal responses. *Soft Matter* **10**, 3027–3035 (2014). doi:10.1039/c3sm52454j Medline

83. D. J. Strickland, L. Zhang, Y.-R. Huang, D. J. Magagnosc, D. Lee, D. S. Gianola, Synthesis and mechanical response of disordered colloidal micropillars. *Phys. Chem. Chem. Phys.* **16**, 10274–10285 (2014). doi:10.1039/C3CP55422H Medline

84. C. F. Brooks, G. G. Fuller, C. W. Frank, C. R. Robertson, An interfacial stress rheometer to study rheological transitions in monolayers at the air-water interface. *Langmuir* **15**, 2450–2459 (1999). doi:10.1021/la980465r

85. S. Reynaert, P. Moldenaers, J. Vermant, Interfacial rheology of stable and weakly aggregated two-dimensional suspensions. *Phys. Chem. Chem. Phys.* **9**, 6463–6475 (2007). doi:10.1039/b710825g Medline

86. N. C. Keim, P. E. Arratia, Mechanical and microscopic properties of the reversible plastic regime in a 2D jammed material. *Phys. Rev. Lett.* **112**, 028302 (2014). doi:10.1103/PhysRevLett.112.028302 Medline

87. N. C. Keim, P. E. Arratia, Role of disorder in finite-amplitude shear of a 2D jammed material. *Soft Matter* **11**, 1539–1546 (2015). doi:10.1039/C4SM02446J Medline

88. A. D. Gopal, D. J. Durian, Relaxing in foam. *Phys. Rev. Lett.* **91**, 188303 (2003). doi:10.1103/PhysRevLett.91.188303

89. A. D. Gopal, D. J. Durian, Shear-induced “melting” of an aqueous foam. *J. Colloid Interface Sci.* **213**, 169–178 (1999). doi:10.1006/jcis.1999.6123 Medline

90. A. Saint-Jalmes, D. J. Durian, Vanishing elasticity for wet foams: Equivalence with emulsions and role of polydispersity. *J. Rheol.* **43**, 1411–1422 (1999). doi:10.1122/1.551052

91. W. Li, J. M. Rieser, A. J. Liu, D. J. Durian, J. Li, Deformation-driven diffusion and plastic flow in amorphous granular pillars. *Phys. Rev. E* **91**, 062212 (2015). doi:10.1103/PhysRevE.91.062212 Medline

92. J. M. Rieser, P. E. Arratia, A. G. Yodh, J. P. Gollub, D. J. Durian, Tunable capillary-induced attraction between vertical cylinders. *Langmuir* **31**, 2421–2429 (2015). doi:10.1021/la5046139 Medline

93. J. M. Rieser, C. P. Goodrich, A. J. Liu, D. J. Durian, Divergence of Voronoi cell anisotropy vector: A threshold-free characterization of local structure in amorphous materials. *Phys. Rev. Lett.* **116**, 088001 (2016). doi:10.1103/PhysRevLett.116.088001 Medline

94. M. Houssais, C. P. Ortiz, D. J. Durian, D. J. Jerolmack, Onset of sediment transport is a continuous transition driven by fluid shear and granular creep. *Nat. Commun.* **6**, 6527 (2015). doi:10.1038/ncomms7527 Medline

95. M. Houssais, C. P. Ortiz, D. J. Durian, D. J. Jerolmack, Rheology of sediment transported by a laminar flow. *Phys. Rev. E* **94**, 062609 (2016). doi:10.1103/PhysRevE.94.062609 Medline

96. Y. F. Bruno Andreotti, O. Pouliquen, *Granular Media: Between Fluid and Solid* (Cambridge Univ. Press, 2013).

97. C. S. O'Hern, L. E. Silbert, A. J. Liu, S. R. Nagel, Jamming at zero temperature and zero applied stress: The epitome of disorder. *Phys. Rev. E* **68**, 011306 (2003). doi:10.1103/PhysRevE.68.011306 Medline

98. C. P. Ortiz, K. E. Daniels, R. Riehn, Nonlinear elasticity of microsphere heaps. *Phys. Rev. E* **90**, 022304 (2014). doi:10.1103/PhysRevE.90.022304 Medline

99. A. J. Liu, S. R. Nagel, The Jamming transition and the marginally jammed solid. *Annu. Rev. Condens. Matter Phys.* **1**, 347–369 (2010). doi:10.1146/annurev-conmatphys-070909-104045